

The Impact of the QBO on MJO Convection in Cloud-Resolving Simulations

ZANE MARTIN AND SHUGUANG WANG

Department of Applied Physics and Applied Mathematics, Columbia University, New York, New York

JI NIE

Department of the Atmospheric and Oceanic Sciences, Peking University, Beijing, China

ADAM SOBEL

*Department of Applied Physics and Applied Mathematics, Columbia University, New York,
and Lamont-Doherty Earth Observatory, Columbia University, Palisades, New York*

(Manuscript received 25 June 2018, in final form 12 November 2018)

ABSTRACT

This study examines the relationship between the Madden–Julian oscillation (MJO) and the stratospheric quasi-biennial oscillation (QBO) in a limited-area cloud-resolving model with parameterized large-scale dynamics. The model is used to simulate two consecutive MJO events that occurred during the late fall and early winter of 2011. To test the influence of the QBO on the simulated MJO events, various QBO states are imposed via the addition of characteristic wind and temperature anomalies. In experiments with only QBO temperature anomalies imposed (without corresponding zonal wind anomalies) the strength of convection during MJO active phases is amplified for the QBO easterly phase [an anomalously cold tropical tropopause layer (TTL)] compared to the westerly QBO phase (a warm TTL), as measured by outgoing longwave radiation, cloud fraction, and large-scale ascent. This response is qualitatively consistent with the observed MJO–QBO relationship. The response of precipitation is weaker, and is less consistent across variations in the simulation configuration. Experiments with only imposed QBO wind anomalies (without corresponding temperature anomalies) show much weaker effects altogether than those with imposed temperature anomalies, suggesting that TTL temperature anomalies are a key pathway through which the QBO can modulate the MJO. Sensitivity tests indicate that the QBO influence on MJO convection depends on both the amplitude and the height of the QBO temperature anomaly: lower-altitude and larger-amplitude temperature anomalies have more pronounced effects on MJO convection.

1. Introduction

The Madden–Julian oscillation (MJO) is the dominant mode of intraseasonal variability in the tropical troposphere and is marked by a planetary-scale organization of deep convection and circulation (Madden and Julian 1994; Zhang 2005). Consisting of an “active” phase associated with increased convection and a corresponding “suppressed” phase associated with decreased convection, the MJO propagates eastward from the Indian Ocean through the west Pacific on time scales of around 30–60 days. In contrast, the quasi-biennial oscillation (QBO) is the main source of interannual variability in the tropical stratosphere (Baldwin et al.

2001). Its prevailing signal is an approximately 28-month cycle in which the tropical stratospheric zonal wind reverses direction, alternating between easterly (QBOE) and westerly (QBOW) phases. These alternating regimes form in the upper stratosphere and descend to the tropical tropopause layer (TTL) at a rate of around 1 km month^{-1} . The QBO also possesses a clear temperature signal in both tropical and extratropical regions that largely follows thermal wind balance (Baldwin et al. 2001). Likely because they occur on different time scales and occupy largely distinct parts of the atmosphere, the MJO and QBO were considered independent by most until recent discoveries by Yoo and Son (2016) and others showed a strong MJO–QBO connection in boreal winter. Here, we present a modeling study aimed at understanding the physics of this connection.

Corresponding author: Zane Martin, zkm2102@columbia.edu

A relationship between the QBO and the MJO was first noted by Kuma (1990), who found that the intensity of upper-tropospheric winds associated with the MJO was well correlated with the QBO. Little subsequent work was done until more recent studies, beginning with Yoo and Son (2016), spurred renewed interest in the topic (Yoo and Son 2016; Marshall et al. 2017; Son et al. 2017; Hood 2017; Nishimoto and Yoden 2017; Lee and Klingaman 2018; Zhang and Zhang 2018; Hendon and Abhik 2018; Wang et al. 2018).

Yoo and Son (2016), through examining QBO and MJO indices, found a significant correlation indicating that the boreal winter MJO is stronger during QBOE and weaker in QBOW. Notably, the correlation was not significant in other seasons. Son et al. (2017) and Nishimoto and Yoden (2017) provided additional evidence for the MJO–QBO connection and described it in more detail through composite analyses of the MJO during different QBO phases. These and other studies have found that during QBOE winters, the MJO tends to propagate slower, last longer, and display stronger teleconnections (Son et al. 2017; Nishimoto and Yoden 2017; Marshall et al. 2017; Wang et al. 2018). Marshall et al. (2017) demonstrated an MJO–QBO relationship in a numerical weather prediction model and further showed that MJO prediction, measured by the lead time that the bivariate correlation of an MJO index remained above 0.5, improved by approximately a week in QBOE versus QBOW. Recently, Zhang and Zhang (2018) have argued that the QBO does not directly modulate the strength of active MJO events; instead there are more active MJO days in QBOE and the MJO propagates more frequently through the Maritime Continent, often lasting longer.

While these studies demonstrate a link between the MJO and the QBO, none of them clearly establishes the physical mechanism connecting the two phenomena. Several such mechanisms have been proposed, however, including a QBO temperature stratification effect, cloud-radiative feedbacks, and a QBO wind shear effect. Of these, the QBO temperature stratification effect is perhaps the most plausible (Hendon and Abhik 2018). It asserts that QBO temperature anomalies modify the thermal stratification in the TTL, destabilizing the atmosphere during QBOE and promoting more vigorous deep convection (and vice versa during QBOW). Previous works examining the QBO's effect on tropical mean convection (not necessarily associated with the MJO) have identified QBO temperature anomalies as a pathway to modulate convection (Gray et al. 1992a,b; Giorgetta et al. 1999; Collimore et al. 2003; Garfinkel and Hartmann 2011; Liess and Geller 2012; Nie and Sobel 2015).

In addition to the QBO's direct temperature stratification effect, cloud-radiative feedbacks may be a further driver of the MJO–QBO link. During QBOE, cold TTL temperatures are conducive to the formation of high-altitude cirrus clouds, whereas warm TTL temperatures are less conducive (e.g., Son et al. 2017). Such cirrus clouds may feed back on existing QBO temperature anomalies by cooling locally at high altitudes while warming the atmosphere below (Hartmann et al. 2001; Yang et al. 2010; Hong et al. 2016). This may reduce the column-integrated radiative cooling, which in turn can increase large-scale ascent and precipitation [i.e., Nie and Sobel (2015); note this is opposite to strict radiative-convective equilibrium regimes, in which a reduction in radiative cooling implies a decrease in precipitation, as here we account for the effects of a large-scale circulation]. As cloud-radiative feedbacks are potentially important for the maintenance of the MJO (e.g., Bony and Emanuel 2005; Sobel and Maloney 2012, 2013; Crueger and Stevens 2015), this mechanism seems particularly well suited in explaining why the QBO affects MJO-related convection more than tropical mean convection (e.g., Son et al. 2017, their Fig. 1).

Another possible mechanism is related to QBO wind anomalies. Gray et al. (1992a,b) and Collimore et al. (2003) suggested that QBO wind anomalies may influence tropical convection via changes in the TTL vertical wind shear, which may shear off convecting cloud tops or otherwise affect convection. Apart from this type of mechanism, which couples QBO wind anomalies to convection locally, QBO wind changes can be expected to alter the propagation and dynamics of transient waves excited by the MJO, such as vertically propagating gravity or Kelvin waves. Modulation of vertically propagating waves in the stratosphere through varying vertical wind shear is central to the mechanism of the QBO itself (Lindzen and Holton 1968; Holton and Lindzen 1972; Plumb and McEwan 1978), and it is conceivable that changes to the propagation characteristics of waves in the stratosphere could play a role in the MJO–QBO interaction, to the extent that they can influence the troposphere. Such nonlocal mechanisms are not examined in this work.

This study models the MJO–QBO connection using a numerical model, and explores mechanisms that couple QBO temperature and wind anomalies directly to convection in the local column. We simulate the MJO in a limited-area, cloud-resolving model augmented with parameterized large-scale dynamics, following Wang et al. (2013, 2016), and then examine the impact of the QBO by imposing characteristic QBO anomalies in the simulation. An advantage of this approach is that cloud-resolving simulations avoid the large uncertainty caused

by convective parameterization in climate models. Additionally, imposing QBO anomalies allows us to focus on the QBO's impact on the MJO, and avoid issues simulating the QBO itself, which can cause difficulties in free-running global climate model simulations (e.g., Lee and Klingaman 2018). Such an approach also allows us to examine QBO temperature and wind effects separately, which is difficult in a climate model because of the thermal wind balance constraint. Limitations include the assumptions and uncertainties associated with the parameterization of large-scale dynamics and the necessity of prescribing aspects of the large-scale flow, as described further in section 2.

Following the modeling study of Wang et al. (2016, hereafter W16), we begin by simulating two consecutive, observed MJO events in our model. The specifics of our model configuration, the data and techniques we utilize, and our experimental design are described in section 2. After establishing that our model reproduces the two observed MJO events with reasonable fidelity, we conduct several QBO experiments, loosely following the experimental design of Nie and Sobel (2015). These test whether various QBO temperature and/or wind anomalies influence the simulated convection. The results from these experiments are presented in section 3. Discussion of our results is provided in section 4, and a summary with our conclusions is laid out in section 5.

2. Data, methodology, and model configuration

a. Data and parameterized large-scale dynamics

The observational data used in this study are from two sources: the Cooperative Indian Ocean Experiment on Intraseasonal Variability in the Year 2011/Dynamics of the Madden–Julian oscillation field campaign (CINDY/ DYNAMO or simply DYNAMO; Yoneyama et al. 2013) and the European Centre for Medium-Range Weather Forecasts global interim reanalysis (ERA-Interim; Dee et al. 2011). The DYNAMO data used here consist of 6-hourly radiosonde measurements from 1 October 2011 through 15 December 2011, averaged horizontally over DYNAMO's Northern Sounding Array (NSA), a large region in the central equatorial Indian Ocean marked by four sounding sites (Johnson and Ciesielski 2013; Sobel et al. 2014; Johnson et al. 2015). As the DYNAMO data do not extend above around 21 km, ERA-Interim is utilized to capture the state of the lower to midstratosphere up to around 29 km. To combine these two datasets, the DYNAMO data are linearly merged with 6-hourly ERA-Interim data, which are horizontally averaged over 0° – 6° N, 73° – 80° E (a region closely corresponding to the NSA). Explicitly, at heights z between approximately 18 and 21 km, a generic variable, say $X(z)$,

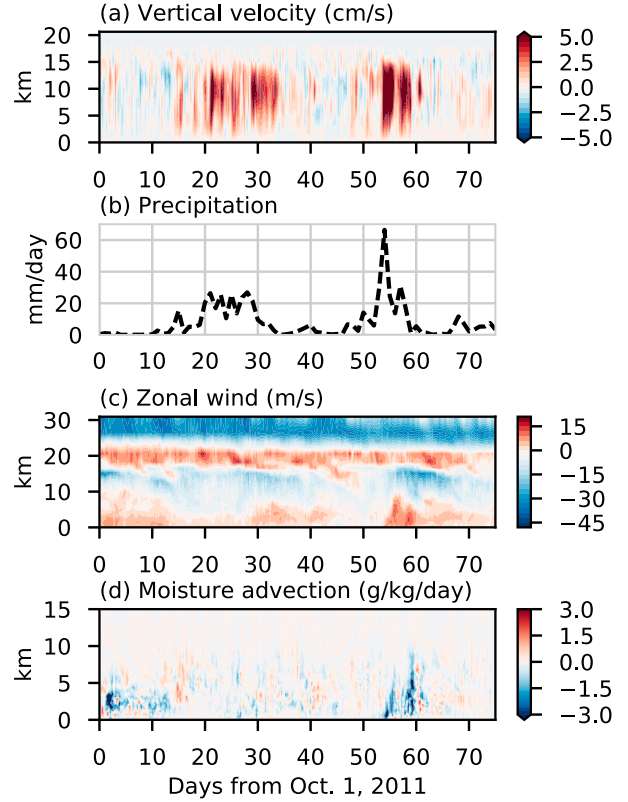


FIG. 1. The DYNAMO–ERA-Interim linearly merged data (as described in section 2a). Plotted are (a) vertical velocity, (b) precipitation (from NSA-derived data), (c) zonal wind, and (d) horizontal moisture advection. All fields are averaged over the DYNAMO Northern Sounding Array, or in ERA-Interim over 0° – 6° N, 73° – 80° E. Horizontal moisture advection is plotted only up to 15 km, as it is set to zero above that point (per section 2c). Days are relative to 1 Oct 2011; the last day is 15 Dec 2011.

is expressed as $X(z) = X_{\text{DYN}}(z)[(21 - z)/(21 - 18)] + X_{\text{ERA}}(z)[(z - 18)/(21 - 18)]$, where X_{DYN} and X_{ERA} are the horizontally averaged values of X in the DYNAMO and ERA-Interim datasets, respectively. This linear merging is done for both the wind and the temperature fields. We do not account for any bias within the ERA-Interim data, as we are primarily interested in the response in our model to QBO anomalies. For ease of reference, this combined ERA-Interim–DYNAMO dataset is referred to simply as “the DYNAMO data.”

Figure 1 shows the vertical velocity, precipitation, zonal wind, and horizontal moisture advection from the DYNAMO data. During the fall and early winter of 2011, two MJO events passed through the NSA. The active phases of these events are evident both in the strong ascent through the troposphere and the increased precipitation centered around days 25 and 55. Additionally, the suppressed phase from around days 30 to 50 shows decreased precipitation and weak descent.

Also notable in Fig. 1 are the QBO signals in stratospheric zonal wind: the QBO at 50 hPa (~ 21 km) was westerly in October and November and neutral by December 2011 (see further in section 2d).

The DYNAMO data are coupled to our cloud-resolving model following a method outlined in W16. The key step is to derive the large-scale vertical velocity using the weak temperature gradient approximation (WTG) discussed below (Sobel and Bretherton 2000; Raymond and Zeng 2005; Sessions et al. 2010; Wang and Sobel 2011). The model is also constrained by the DYNAMO data in other aspects. The horizontally averaged model zonal and meridional winds are relaxed uniformly at each model level toward the DYNAMO wind profile with a relaxation time of 1 h. The lower boundary condition of the model is a horizontally uniform daily sea surface temperature taken from OAFlux, a product that uses optimal analysis to combine both reanalysis and satellite products (Yu and Weller 2007; Yu et al. 2008). The horizontal advection of moisture into the model domain implied by the large-scale zonal and meridional flow is specified by imposing an additional tendency term to the moisture budget consistent with this advection (Fig. 1d), at times forcing the model with significant low-level drying associated with westerly winds (Sobel et al. 2014). This large-scale horizontal moisture advection is held fixed regardless of the parameterized large-scale vertical velocity. While methods for parameterizing the large-scale horizontal moisture advection have been used occasionally in other modeling studies (Raymond and Zeng 2005; Sobel et al. 2007), W16 showed that such methods were insufficient in this context (W16, see their appendix A).

b. Spectral weak temperature gradient based on vertical structure

Limited-area cloud-resolving simulations are typically driven by prescribing the large-scale vertical wind and the vertical advective tendencies, a method that is useful for studying convective characteristics (e.g., Grabowski et al. 1996; Wu et al. 1998; Tao et al. 2004; Blossey et al. 2007; Wang et al. 2015; Li et al. 2018). However, as specifying these fields may misrepresent causality related to convection and circulation (Mapes 1997, 2004), methods have been developed to parameterize the large-scale vertical velocity and vertical tendencies (e.g., Sobel and Bretherton 2000; Raymond and Zeng 2005; Kuang 2008; Romps 2012a, b; Wang et al. 2013; Herman and Raymond 2014; Edman and Romps 2015; Nie and Sobel 2016; W16). An intercomparison using two such methods with many different models in idealized simulations can be found in Daleu et al. (2015, 2016). Following in particular W16 and Herman and Raymond

(2014), here we utilize one such technique, known as the vertical-mode-based spectral weak temperature gradient method (SWTG).

Horizontal temperature gradients in the tropical troposphere are small because local temperature anomalies are quickly removed by gravity waves (Charney 1963; Held and Hoskins 1985; Bretherton and Smolarkiewicz 1989). The WTG method for single-column and limited-domain cloud-resolving modeling (Sobel and Bretherton 2000; Raymond and Zeng 2005) assumes that the large-scale vertical velocity w maintains this homogeneity in temperature by restoring the virtual potential temperature θ to some reference profile $\bar{\theta}_{\text{ref}}$. Mathematically, this can be represented via a truncation of the temperature equation as follows:

$$\bar{w} \frac{\partial \bar{\theta}}{\partial z} = [\bar{\theta} - \bar{\theta}_{\text{ref}}(z, t)]/\tau, \quad (1)$$

where the overbar indicates horizontal averaging. Here τ is a relaxation time scale, usually on the order of hours, associated with how quickly gravity waves propagate through the domain. For this study we set $\tau = 1$ h. Note in Eq. (1), $\bar{\theta}_{\text{ref}}$ is a function of height, as is typical, but is also time dependent. While this is not often the case in WTG experiments, several recent studies have demonstrated its viability (e.g., Wang et al. 2013; Sentić et al. 2015; W16; Sessions et al. 2016). Following W16, $\bar{\theta}_{\text{ref}}$ is not taken directly from the DYNAMO data, but is calculated from a model run with imposed vertical velocity, as this improves simulations by explicitly considering model bias (Edman and Romps 2014; W16). Within the model, Eq. (1) is solved for w throughout the free troposphere, and the resulting large-scale or “WTG” vertical velocity is used to advect moisture and temperature. In this way, we capture the effects of the large-scale circulation on these fields, and allow convection to vary during the simulation in a realistic way.

Here we use the spectral weak temperature gradient method developed by Herman and Raymond (2014) as modified by W16. We solve Eq. (1) by first decomposing the vertical velocity into a sum of vertical modes, each with an associated vertical structure and phase speed. We then assume that WTG holds for each mode, and further that the i th mode has a characteristic time scale, say τ_i , inversely proportional to its phase speed. Following W16 (their section 2.2.3), we calculate these modes from the vertical profile of the Brunt–Väisälä frequency by solving a vertical structure equation with specified boundary conditions (e.g., Fulton and Schubert 1985; Wu et al. 2000; Bergman and Sardeshmukh 2004; Mapes 2004; Tulich et al. 2007). Once the modes are calculated, the right-hand side of Eq. (1) is projected

onto the vertical modes, and the large-scale vertical velocity field is then obtained by solving Eq. (1) for each mode and then summing over the modes to obtain the total w .

We utilize this vertical-mode-based SWTG methodology because it is conceptually appealing, produces smooth vertical velocity profiles, and leads to the most realistic structures of large-scale ascent and rain in the DYNAMO MJO events compared to other large-scale parameterizations (W16). The N^2 profile used to calculate the modes is the time mean from the DYNAMO data. We use the first 20 modes, and assume a rigid lid boundary condition in the vertical velocity at 20 km. The sensitivity to the rigid lid height is explored in the appendix where it is set to 16 km.

c. Numerical model and forcing

Our cloud-resolving simulations use the WRF Model, version 3.5.1 (Skamarock et al. 2008), the same model and version as W16. The setup also largely follows W16 and is broadly similar to other WTG studies (e.g., Wang et al. 2013; Sentić et al. 2015; Edman and Romps 2014). The horizontal domain is 64 km by 64 km with a 1-km resolution and doubly periodic lateral boundary conditions. To better represent the lower stratosphere, we improve upon W16 by raising the model top to around 29 km with 89 vertical levels (from the ~22 km used in W16). Following Nie and Sobel (2015), these levels are not uniformly spaced, but vary to include more levels near the surface and the tropopause. There are 20 levels below 5 km with a linearly increasing step size from 75 to 500 m; above 5 km the resolution is 500 m, except from 12 to 20 km where it is 250 m.

We use the Morrison microphysics scheme, which predicts the mixing ratio and number concentration of rain, cloud water, cloud ice, snow, and graupel (Morrison et al. 2009). The radiative fluxes are calculated via the RRTMG longwave scheme (Iacono et al. 2008) and the Goddard shortwave scheme (Chou and Suarez 1999; Matsui et al. 2007; Shi et al. 2010). Insolation at 3°N, 76°E, including the diurnal cycle, is specified uniformly over the domain. An implicit damping is used in the top 6 km of the model domain to suppress gravity wave reflection off the top boundary (Klemp et al. 2008). Subgrid-scale turbulent mixing eddies are parameterized using the 3D Smagorinsky first-order closure scheme (Skamarock et al. 2008). To ensure conservation of moisture, we utilize the implicit vertical diffusion scheme from W16 and similar to Hong et al. (2006). The Coriolis parameter is set to zero, as the NSA is close to the equator and the domain is small relative to the equatorial deformation radius. The model simulation is sampled four times daily.

Following W16, all runs analyzed are initialized on 10 October 2011. In runs initialized on 1 October, the model settles into an unrealistically dry state with no precipitation. This sensitivity to initial moisture leading to “multiple equilibria” has been found in other WTG simulations (Sobel et al. 2007; Sessions et al. 2010). Examining the transition behavior of w in such states suggests that the dry equilibrium originates from an ascent–descent couplet in the middle troposphere (e.g., day 10 in Fig. 3d; Anber et al. 2017). This couplet grows and descends because of interaction between radiation and temperature anomalies under WTG (Mapes and Zuidema 1996; Emanuel et al. 2014). More importantly, it removes moisture from the column, and the system settles into the dry state. In our tests, initialization on 10 October largely avoids this issue, though non-precipitating states occur in one experiment discussed below. Model initial conditions of moisture, temperature, winds, and geopotential heights are created with an observed sounding averaged over the NSA and including ERA-Interim data in the lower stratosphere. To break symmetry, uniformly distributed random noise of magnitude 2 K is added to the initial potential temperature field in the bottom 10 levels. This also permits us to carry out ensembles of integrations to better distinguish signal from noise. As a result, the individual convective systems simulated differ across ensemble members (not shown). This method does not, on the other hand, generate a large spread in horizontally averaged quantities (e.g., rain rate or vertical profile of temperature), presumably because of the lack of spread in the domain-mean forcing. Thus, the spread generated should not be considered to represent the full dynamical uncertainty in the way that ensemble forecasts using global models can.

Two additional modifications were made from W16 because of our higher model top. First, the temperature and winds in the stratosphere (above 20 km) are relaxed on a 1-h time scale toward the reference virtual potential temperature to prevent unrealistic drift. Additionally, large-scale horizontal advection of moisture above 15 km is set to zero, as in some integrations the imposed drying led to unphysical negative moisture values. As the actual forcing is already near zero at these levels, this change has a negligible effect on the simulations without negative moisture values.

d. Experimental design

We track the QBO using ERA-Interim monthly zonal-mean zonal wind at 50 hPa (U50), averaged over the tropics (10°N–10°S and all longitudes) from January 1979 to June 2017. Months when U50 is greater than or less than half of its standard deviation are defined as QBOW and QBOE, respectively, following

[Yoo and Son \(2016\)](#) and [Son et al. \(2017\)](#). During the DYNAMO period, the QBO was westerly during October and November and neutral by December 2011. Note too that the DYNAMO events studied here occurred in the fall and early winter, whereas the observed MJO–QBO relationship seems primarily limited to December–February ([Yoo and Son 2016](#); [Son et al. 2017](#)). Despite both the existing QBO state and the season, we treat the simulated DYNAMO MJO events as a “control” simulation.

$$A'_{u,t}(z) = \begin{cases} \pm M_{u,t} \{1 - [(z - z_o)/H]^2\}, & \text{if } z_o - H < z < z_o + H \\ 0, & \text{otherwise.} \end{cases} \quad (2)$$

Here $A'_{u,t}$ is the anomaly, $M_{u,t}$ is the amplitude of the anomaly, and the subscript denotes zonal wind or temperature. The plus-or-minus symbol indicates positive or negative anomalies, respectively, though in some cases the magnitude of the QBOE and QBOW anomalies are not symmetric. For the QBO wind anomalies, the values of M_u used are -15 and 10 m s^{-1} for QBOE and QBOW, respectively. For the temperature anomalies, the values of M_t are symmetric and are either ± 1 , ± 0.5 , or $\pm 2 \text{ K}$, where indicated below; in most runs $M_t = \pm 1 \text{ K}$. The anomaly peaks at height z_o , and it is symmetric in the vertical between $z_o - H$ and $z_o + H$, so that H is the half depth of the QBO anomaly. The peak height of the anomaly varies across different runs: QBO temperature anomalies vary z_o from 16 to 20 km, and QBO wind anomalies vary z_o from 18 to 22 km, both in 1-km increments. In all our experiments the half depth is fixed at $H = 4 \text{ km}$. Note that observed QBO signals in the middle to upper stratosphere are not included in our idealized anomalies, as it seems unlikely that such high-altitude anomalies could affect convection (see [section 3c](#) for validation).

Although the observed QBO anomalies are not strictly parabolic with height, we calculated approximate values of $M_{u,t}$ and z_o from the ERA-Interim data to facilitate comparison with our input model values. To do this, we found both the minimum and maximum amplitude of the QBOE and QBOW anomalies in the TTL (i.e., $< 24 \text{ km}$) and the height at which those extrema occurred, quantities somewhat analogous to $M_{u,t}$ and z_o . For ERA-Interim, $z_o = 18.6 \text{ km}$ for temperature and 20.6 km for wind, though the vertical resolution of ERA-Interim in the TTL is coarse (varying between ~ 1 and 3 km from 14 to 23 km). The value of M_t is 0.81 K for QBOW and -0.78 K for QBOE, and M_u is -15.8 m s^{-1} for QBOE and 9.8 m s^{-1} for QBOW.

To impose the idealized QBO states, we add the QBO anomalies, derived as described above, to the DYNAMO

We now describe the QBO anomalies we impose upon this control simulation. We first composited vertical profiles of tropical-averaged zonal-mean temperature and zonal wind in QBOE and QBOW from ERA-Interim monthly data. The anomalies relative to the time mean are plotted in [Fig. 2](#). Following [Nie and Sobel \(2015\)](#), we then create a range of idealized temperature and wind anomalies as parabolas with a peak amplitude approximately equal to the observed QBO signal, written as follows:

large-scale forcing data during the entire simulation period (which, recall, is weakly QBOW to QBO neutral). While observed QBO anomalies descend at a rate of around 1 km month^{-1} , our anomalies are fixed during each simulation. The QBO anomalies were not added to the initial conditions in the results shown here, as this sometimes led to the model’s settling into the nonprecipitating state discussed above (not shown). While this itself suggests that conditions in the TTL can influence MJO-related convection, the occurrence of these states is in strong contrast to observations and precludes comparison to other runs.

We design three types of experiments to test the mechanisms discussed in the introduction: 1) those in which only the large-scale temperature field is modified with QBOE or QBOW signals, 2) those in which only the large-scale wind is modified, and 3) those in which QBO temperature and wind signals are both included. To explore the sensitivity to the height and amplitude of the QBO anomaly, in [section 3c](#) we consider a range of values for M_t and z_o . This sensitivity testing accounts in part for differences in the shape of the QBO anomaly that may depend on, for example, our particular QBO index, reanalysis product, and lack of bias correction. A summary of all the experiments presented in this paper is provided in [Table 1](#).

3. Results

a. Control runs

Our control runs are comparable to [W16](#)’s simulations with interactive radiation (their section 3.2), albeit with a higher model top and higher vertical resolution. [Figure 3](#) shows the results from control simulations with five ensemble members, with ensemble spread (shading in [Figs. 3a and 3b](#)) due to the white noise in the initial

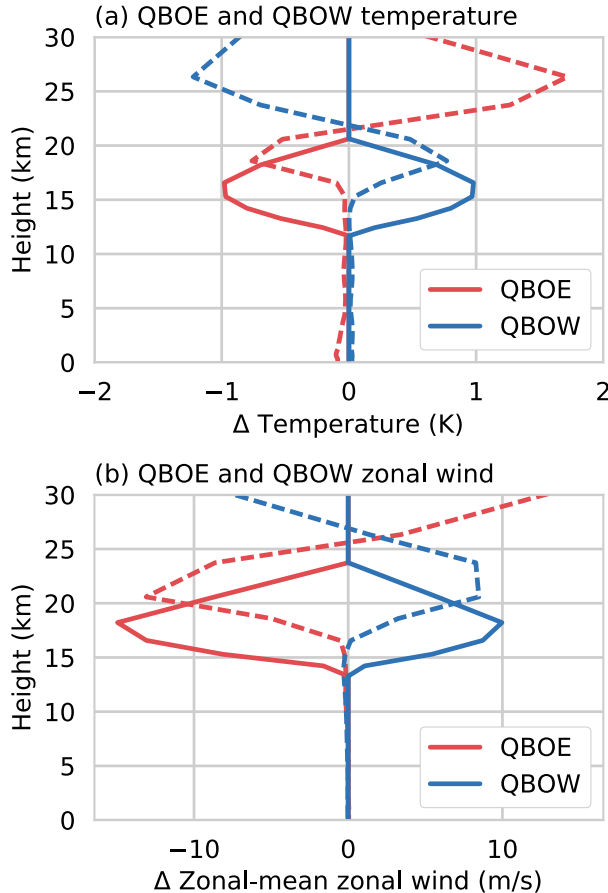


FIG. 2. Idealized (solid) and observed (dashed) QBO (a) temperature and (b) zonal wind anomalies averaged over the tropics (10°N – 10°S and all longitudes). The observed anomalies are calculated using a 50-hPa QBO index based on ERA-Interim monthly data, as described in section 2d. The idealized anomaly is parabolic per Eq. (2); here the peak is plotted at 16 km for the temperature anomaly and 18 km for the wind anomalies. The idealized anomaly is plotted after interpolation onto the DYNAMO forcing levels, which accounts for the vertical asymmetry about the peak in (b).

temperature field. Comparisons of the model and observations in Fig. 3 show that the control runs simulate the two MJO active phases with reasonable fidelity. The model reproduces both the periods of increased precipitation associated with the active phases, though the large observed spike of precipitation around day 55 is missed in the model, and the second MJO event develops later in the model than in observations. The dry, suppressed phase is also well-simulated, and evident from around day 35 to day 55.

The SWTG vertical velocity is in good agreement with the observed (Figs. 3c,d): the model captures the periods of ascent during the active phases and the weak descent in the suppressed phase. The magnitude of the SWTG vertical velocity is often larger than the observed, however,

and the structure is more top-heavy. The model displays a descending couplet (ascent in the upper troposphere and descent in the lower troposphere) around day 45, a feature that is inconsistent with the observations and can lead to unusually strong precipitation and/or low OLR. W16 and Anber et al. (2017) noted this feature in their simulations with interactive radiation as well.

Unlike the precipitation and vertical velocity, the model OLR differs more substantially from the observations (Fig. 3b), especially during the first MJO event, where the disagreement reaches tens of watts per square meter. The model OLR during the second MJO event is in closer agreement with the observations, though again the model MJO active phase begins later than the observed. The OLR also has an unrealistic dip in the model around days 40–45 corresponding to the descending couplet. We conclude that the model reproduces the observed MJO events reasonably well despite the discrepancies described above. Our results are not substantially different from those of W16 despite our modifications to the model and experimental setup.

b. QBO experiments

In this section we present results from simulations in which we impose various QBOE or QBOW anomalies. We begin by only modifying the temperature field, before discussing the wind-only experiments and then the combined wind and temperature experiments. We first impose a QBOE or QBOW anomaly with amplitude $M_t = \pm 1\text{ K}$, with a peak z_o at 16 km, extending down to 12 km and up to 20 km. These QBOE and QBOW idealized anomalies are shown in Fig. 2.

The idealized temperature anomalies in this section are lower in altitude by around 2.5 km than those observed and have larger values of the vertical depth H . The sensitivity of our results to these differences is explored more in section 3c, but in brief, it is likely that both the QBO forcing and the model response in these runs are stronger than in observations. We nevertheless include this stronger QBO temperature forcing, in large part because of the clearer MJO response shown below. Section 3c discusses this issue in more detail.

As with the control, the QBOE and QBOW simulations are each performed with five ensemble members. The results are shown in Figs. 4–6. These temperature-only experiments generally demonstrate an MJO response to the QBO that is qualitatively consistent with the observed MJO–QBO link: the model shows stronger MJO-associated convection in QBOE compared to QBOW. Figure 4 shows the time series of precipitation and OLR for the three QBO states: QBOE, QBOW, and the control. The OLR is consistently lower (higher) in QBOE (QBOW), while the precipitation is higher in

TABLE 1. List of experiments. The first column indicates what type of QBO anomaly was imposed; control indicates no anomaly. The second and third columns correspond to the height of the anomaly's peak z_0 and its amplitude $M_{u,t}$ per Eq. (2). Commas indicate separate experiments. For temperature and wind experiments, the height is listed in the form: “temperature anomaly peak height”/“wind anomaly peak height.” The fourth column lists the number of ensemble members. The final column indicates the main section where the run is discussed.

Type	z_0 (km)	$M_{u,t}$	Ensemble size	Section
Control	—	—	5	3a
Temperature	16	± 1 K	5 QBOE and 5 QBOW	3b
Temperature	16, 17, 18, 19, 20	± 1 K	1 QBOE and 1 QBOW per height	3c(1)
Temperature	18	± 1 K	5 QBOE and 5 QBOW	3c(1)
Wind	18, 19, 20, 21, 22	10 and -15 m s^{-1}	1 QBOE and 1 QBOW per height	3c(1)
Temperature and wind	16/18, 17/19, 18/20, 19/21, 20/22	± 1 K, $+10$ and -15 m s^{-1}	1 QBOE and 1 QBOW per height	3c(1)
Temperature	16	$\pm 0.5, \pm 2$ K	1 QBOE and 1 QBOW per amplitude	3c(2)
16-km rigid lid: Control	—	—	5	Appendix
16-km rigid lid: Temperature	16	± 1 K	5 QBOE and 5 QBOW	Appendix

QBOE and lower in QBOW; both are in keeping with enhanced convection during QBOE. The large-scale vertical velocity and cloud fraction are also consistent with stronger MJO convection during QBOE, as shown in Fig. 5. The time-mean quantities show that from around 5 to 15 km the vertical velocity is stronger in QBOE and weaker in QBOW. The same can be said of the cloud fraction; in particular, the changes to high clouds are in keeping with the observed MJO–QBO interaction (e.g., Son et al. 2017). Figure 5 also shows a downward-sloping pattern in the QBOE–QBOW changes to cloud fraction, indicating that changes to high clouds precede deeper, midtropospheric cloud changes (see days 25–35 and days 45–55).

Across all variables, the time series show that QBOE–QBOW differences are most pronounced during the MJO active phases, while differences are typically small during the suppressed phase. This suggests, as one might expect, that only convection capable of reaching the level of the QBO anomaly is modulated by the temperature changes. The pronounced changes in the active phase and lack of change in the suppressed phase also demonstrate that QBO temperature anomalies modulate not only the model's mean state, but the amplitude of the variability associated with the MJO, as discussed more below.

Figure 6 shows the ensemble-averaged QBOE–QBOW potential temperature in the simulations; Fig. 6b compares the model time-mean to the input idealized QBO potential temperature anomaly (note here we plot potential temperature, not temperature as in Fig. 2). The model potential temperature difference in the time mean is stronger (i.e., more negative) than the input anomaly around the tropopause by around 0.4 K, which amounts to $\sim 10\%$ of the time-mean value (around -4 K). This suggests that

some process in the tropopause region acts to enhance the existing QBO anomaly. The time series in Fig. 6a further shows that these enhanced temperature signals are largest during MJO active phases, as evident around days 20–35 and days 50–60 where differences reach a

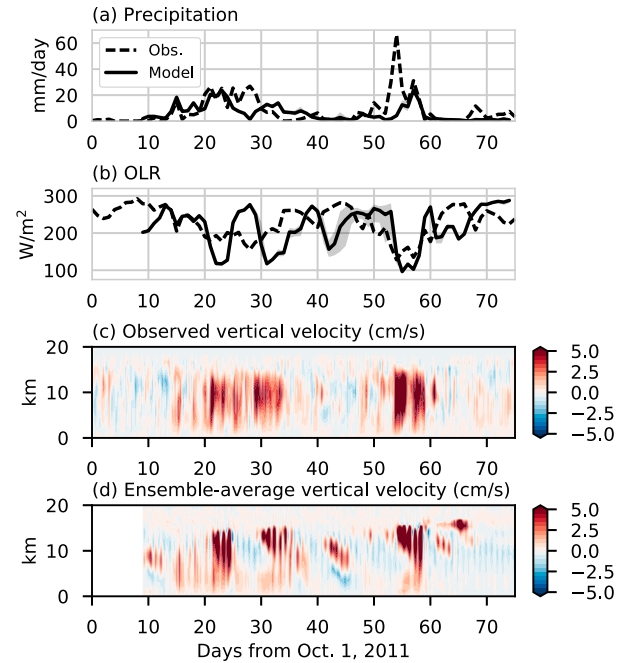


FIG. 3. Control simulations compared to observations for horizontally averaged (a) precipitation (mm day^{-1}), (b) OLR (W m^{-2}), and (c),(d) vertical velocity (cm s^{-1}). In (a) and (b), shading denotes the spread among ensemble members, defined throughout as the minimum and maximum values across all ensemble members at each time step. The solid black line is the model ensemble average and the dashed line is the observed. The model is initialized on 10 Oct 2011 per section 2c, hence the white space preceding day 9.

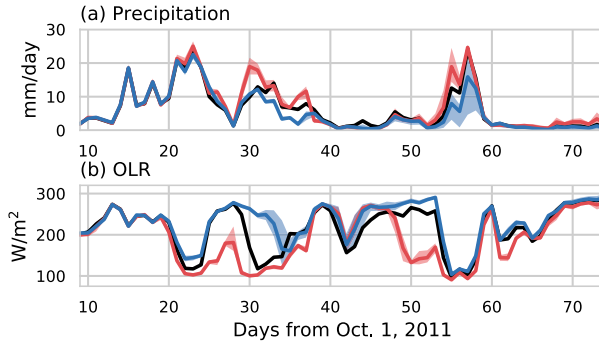


FIG. 4. (a) Precipitation and (b) OLR from model integrations with no QBO anomaly (black), a QBOE temperature anomaly (red), and a QBOW temperature anomaly (blue). As before, the shading denotes ensemble spread and the bold is the ensemble average; the spread in the control is not shown. The QBO temperature anomaly is imposed with $z_0 = 16\text{ km}$ and $M_t = \pm 1\text{ K}$ as shown in Fig. 2 and described in section 2d. No QBO wind signal is added.

minimum of around -13 K . These results show that the imposed QBO temperature anomalies enhance coupling between large-scale velocity and convection in such a way as to reinforce the QBO temperature anomalies. These results may also be in keeping with Hendon and Abhik (2018), who examined the MJO's vertical structure under different phases of the QBO and found that the cold cap

around the tropopause associated with the MJO is strengthened by around 0.5 K during QBOE, and similarly weakened during QBOW.

In contrast to the QBO temperature-only simulations, results from experiments in which the wind field was modified with QBO anomalies showed no substantial change across any of the fields of interest, even for lower-than-observed altitude anomalies. Further evidence that wind anomalies have little to no effect on convection is evident in the combined wind and temperature experiments, in which QBO anomalies in both variables were added. Results from these experiments are very similar to the temperature-only experiments, with minor differences that are indistinguishable from noise. Because these differences are small in general, results from both the wind-only and the temperature and wind results are presented only briefly in the following section (see Figs. 7 and 8). This lack of an influence suggests that QBO wind anomalies do not have a direct influence on MJO convection.

c. Sensitivities to the shape of QBO temperature anomaly

In this section we explore the sensitivity of our results to the height and amplitude of the QBO temperature anomaly. As in Nie and Sobel (2015), both parameters

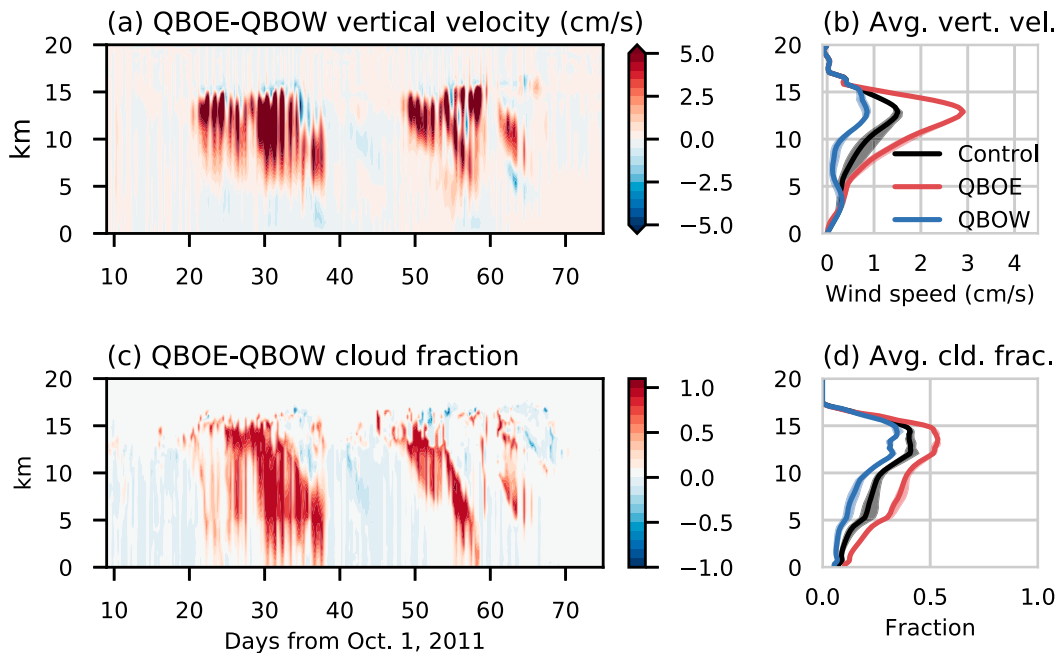


FIG. 5. From the same QBO temperature experiment as in Fig. 4, showing (a),(b) vertical velocity and (c),(d) cloud fraction. (left) The ensemble-averaged, horizontally averaged QBOE–QBOW difference (red indicates QBOE > QBOW). (right) The time-mean for QBOE, QBOW, and the control; the shading indicates ensemble spread. Here and throughout, cloud fraction is calculated as the fraction of grid points with cloud water content (cloud water vapor, ice, rain, snow, hail, and graupel) exceeding the minimum of 0.01 g kg^{-1} or 1% of its saturation value.

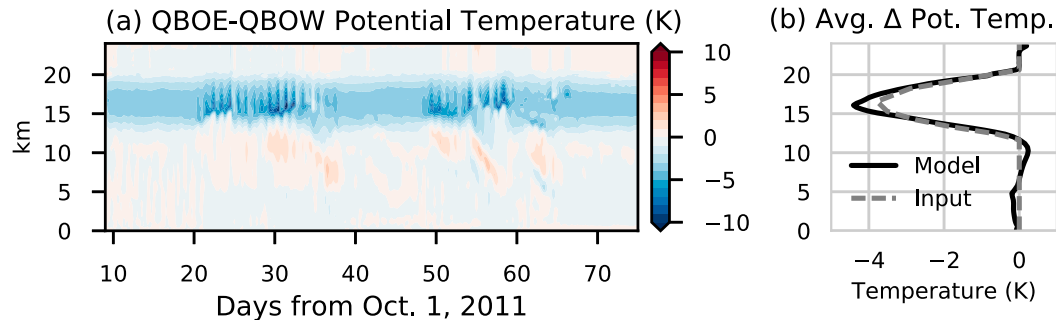


FIG. 6. From the same QBO temperature experiment as in Figs. 4 and 5, showing the potential temperature difference between QBOE and QBOW. (a) The ensemble-averaged, horizontally averaged difference. (b) The time-mean difference (black solid) as well as the idealized QBOE–QBOW temperature anomaly added into the model (gray dashed). Note we plot potential temperature as opposed to temperature, which is shown in Fig. 2. Results are shown up to the level where the model damping begins (24 km).

are found to be important in determining the strength of the QBO influence on the simulated MJO. We also briefly present results from the QBO wind-only and QBO wind and temperature experiments to contrast the relatively small effects of wind anomalies with the effects of temperature anomalies on simulated MJO convection.

1) HEIGHT OF THE QBO ANOMALIES

We first perform a series of one-member integrations in which the height of the QBO anomalies in wind and temperature are varied in 1-km increments. QBO temperature anomalies in these simulations have peak heights z_0 from 16 to 20 km and QBO wind anomalies vary z_0 from 18 to 22 km. The vertical width of the anomaly H in all cases is 4 km; the observed width of the anomaly tends to become thinner as it descends to lower levels, but for simplicity we hold it fixed. The amplitude of the anomalies is also held fixed at ± 1 K for temperature and at -15 and 10 m s^{-1} for QBOE and QBOW winds. When imposed together, the wind anomaly peaks 2 km above the temperature anomaly, roughly consistent with the observed peak-height difference per ERA-Interim. Figures 7 and 8 show the results of the integrations.

Figure 7 shows the QBOE–QBOW difference in the time-mean large-scale vertical velocity and cloud fraction for various experiment types and values of z_0 . The similarity between the temperature-only simulations and the temperature and wind simulations is immediately apparent, as is the lack of a QBO signal in the wind-only integrations. Of more interest is the relationship between the height of the QBO temperature anomaly and the MJO response (Figs. 7a,b). Figures 7a and 7b clearly show that the QBO influence lessens dramatically as the height of the QBO anomaly increases: QBO-induced changes to cloud fraction and

vertical velocity decrease in amplitude and lose a coherent structure. The simulations with z_0 equal to 19 and 20 km in particular lack an obvious QBO response. The run with $z_0 = 18$ km is subtler to diagnose, as it shows a weak but detectable signal. This experiment is discussed in more detail below (see also Figs. 9–11). In addition to the weakening of the QBO influence as z_0 increases, note that the peak of the QBOE–QBOW difference in vertical velocity and cloud fraction shifts upward for higher anomalies and signals in the mid- to lower troposphere weaken. This suggests that the QBO influence is increasingly confined locally as the temperature anomaly moves to higher altitudes.

Figure 8 shows the QBOE–QBOW differences in the time mean and standard deviation of precipitation and OLR as functions of z_0 for the three types of QBO experiment. The x axis indicates the height of the anomaly's peak and the y axis indicates the QBOE–QBOW difference. The OLR results (Figs. 8b,d) are fairly consistent with the cloud fraction and vertical velocity changes described above: there is a small change in the wind experiments, a similarity between the temperature-only and the temperature and wind experiments, and a monotonic relationship between the height of the QBO anomaly and the strength of the MJO convective response. This is true both in the time mean and standard deviation.

Precipitation changes display a less clear or consistent relationship as z_0 is varied, compared to changes in other fields (Figs. 8a,c). Only in the temperature-only experiment with the lowest-altitude forcing ($z_0 = 16$ km) are precipitation signals clearly seen in the time mean or standard deviation. In all the higher-altitude forcing experiments it is difficult to detect a clear QBO-induced signal and the precipitation displays a lack of monotonicity with respect to forcing altitude. We conclude

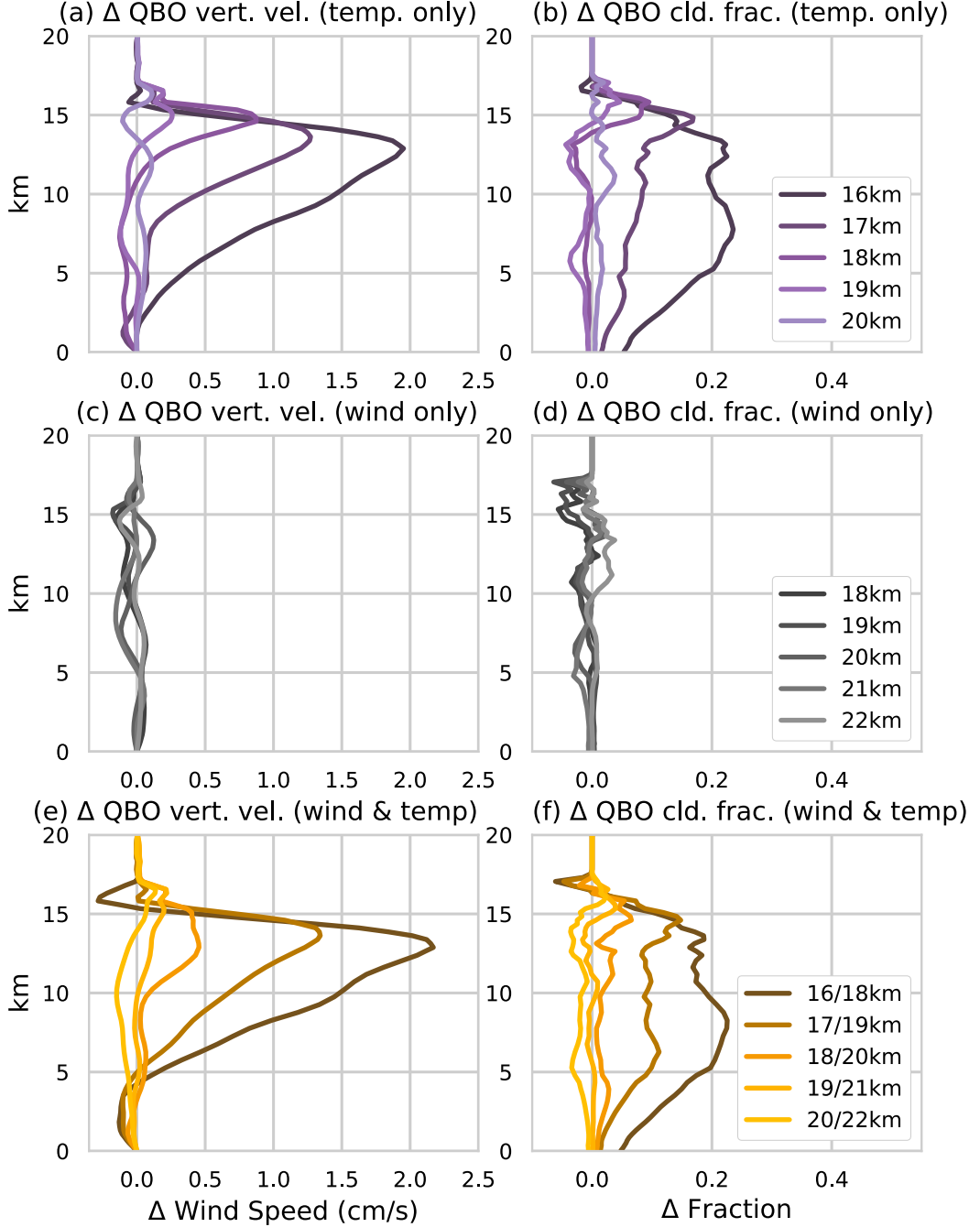


FIG. 7. Time-mean, horizontal-mean QBOE–QBOW differences in (left) vertical velocity and (right) cloud fraction. (a),(b) Temperature-only experiments (purple), (c),(d) wind-only experiments (gray), and (e),(f) combined wind and temperature experiments (gold). Darker colors indicate lower-peaked anomalies; the legend indicates the altitude of the peak of the anomaly z_0 . For the combined temperature and wind experiments, the legend indicates first the height of the peak of the temperature anomaly, then that of the wind anomaly.

that no precipitation signal is clearly present in these QBO experiments. Possible reasons why the MJO–QBO relationship is less apparent in precipitation than in other variables are discussed more in section 4.

To further explore forcing the model with more realistic altitude QBO anomalies, we repeat the 18-km-peaked temperature anomaly simulation including five ensemble members each for QBOE and QBOW.

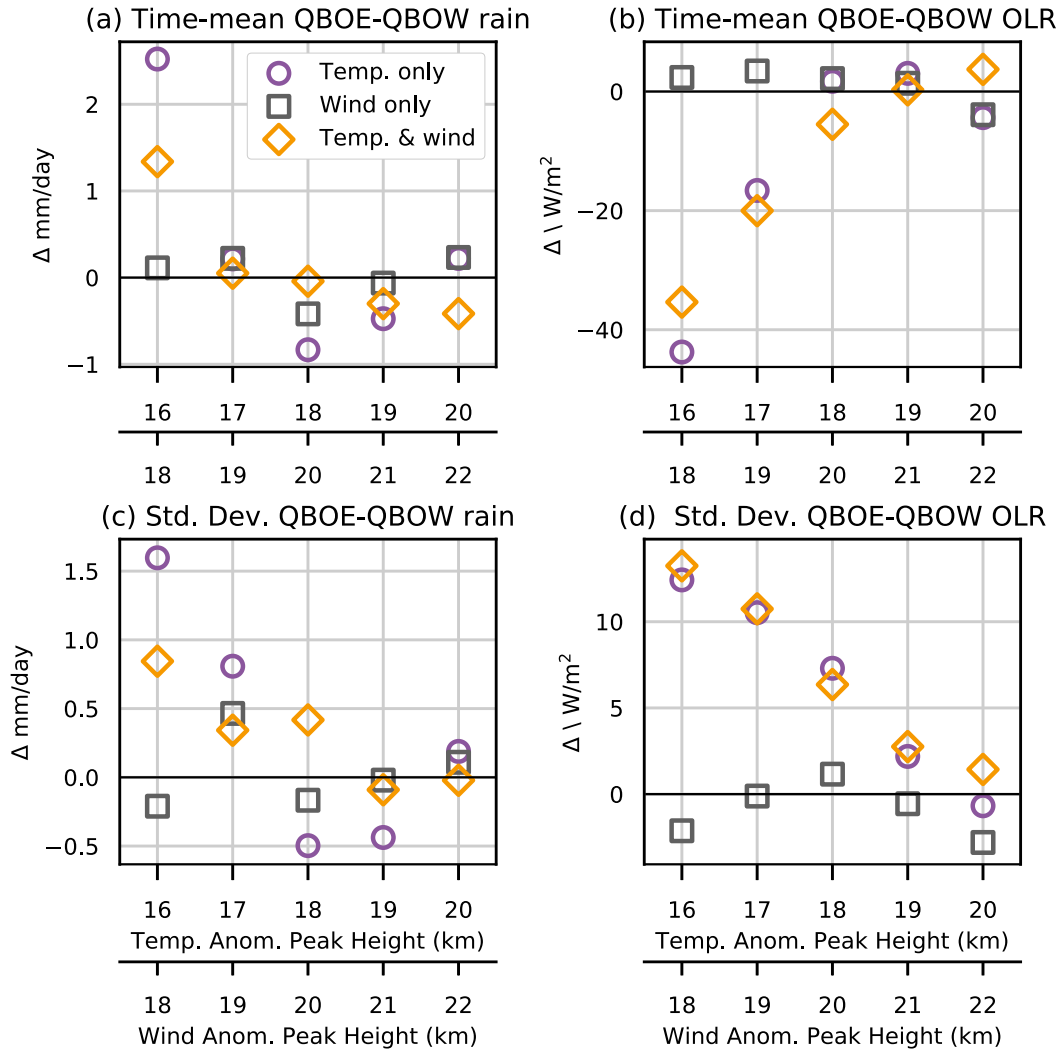


FIG. 8. QBOE–QBOW differences in the (top) time-mean and (bottom) standard deviation of (a),(c) rain and (b),(d) OLR from the same experiments as in Fig. 7. The y axis shows the magnitude of the difference. The x axis is the altitude (km) of the peak of the QBO temperature or wind anomaly: farther right corresponds to higher altitudes. The results are shown for temperature-only experiments (purple circles), wind-only experiments (gray squares), and temperature and wind experiments (gold diamonds).

This allows us to better assess the strength of the signal in the case where the MJO response is small. The results are shown in Figs. 9–11.

Compared to the 16-km-peaked runs, the changes in the model to the 18-km-peaked QBO temperature anomaly are at times difficult to distinguish from noise. In particular, there no longer seems to be a robust or recognizable QBO signal for precipitation in the mean or the time series (Figs. 9 and 11). The QBO influence on OLR, while also much smaller than in the 16-km-peaked temperature experiments, is more consistent across ensemble members, and typically shows a decrease during the MJO active phases in QBOE relative to QBOW (i.e., Fig. 9b from days 30–35 to days 50–55), and a small

increase in the suppressed phase. Both vertical velocity and cloud fraction changes are clearer than OLR or precipitation, and are especially evident during MJO active phases. In the time mean, the changes have the same sign as the 16-km-peaked results, albeit with a smaller magnitude (Fig. 10). In addition, the signal is more localized to the upper troposphere compared to the 16-km run, and is near zero below ~ 10 km in both cloud fraction and vertical velocity.

Figure 11 compares the ensemble QBOE–QBOW spread in the time mean and standard deviation of OLR and precipitation between the 16- and 18-km-peaked runs. This establishes that while time-mean QBOE precipitation is always higher than QBOW precipitation

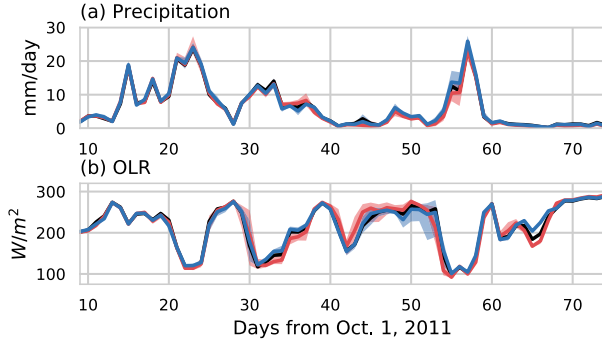


FIG. 9. Horizontally averaged (a) precipitation and (b) OLR from integrations with QBO temperature anomalies that peak at 18 km, as opposed to the 16 km shown in Fig. 4. As in Fig. 4, the shading indicates spread among ensemble members and the thick line is the ensemble average; note that the control spread is not shown.

in the 16-km-peaked runs, the ensemble spread is fairly large; the precipitation signal is absent in the 18-km-peaked simulations. The time-mean QBOE–QBOW OLR changes across ensemble members are also near zero in the 18-km-peaked integrations. However, the 18-km runs do display a signal in the standard deviation of OLR, with an ensemble-mean QBOE–QBOW difference in standard deviation of approximately 5 W m⁻² (Fig. 11d). In this regard, the 18-km-peaked runs may be more consistent with the observed relationship, with a

small change in the mean but a larger signal in the standard deviation (e.g., Son et al. 2017). However, care should be taken in interpreting this result, as it may simply be fortuitous and attributable to the small magnitude of the changes or the short integration period. Additionally, interpretation of this result is complicated by the lack of agreement between simulated and observed OLR, especially during the suppressed phase.

2) AMPLITUDE OF THE QBO TEMPERATURE ANOMALIES

In this section we examine the effect of changing the amplitude of the QBO temperature anomalies. We repeat the simulations from section 3b where $z_0 = 16$ km but include additional experiments either doubling or halving QBO temperature anomaly. Each experiment is conducted with a single ensemble member. The results (Figs. 12 and 13 and Table 2) indicate a monotonic relationship between the amplitude of the QBO temperature anomaly and the strength of the MJO convective response. The QBOE integrations with the greatest amplitude ($M_t = -2$ K, approximately double the observed amplitude) show the lowest OLR, strongest vertical velocity, and highest cloud fraction and precipitation, while those with the strongest QBOW amplitude ($M_t = 2$ K) show the highest OLR, the weakest vertical velocity, and the lowest cloud fraction and precipitation. The QBOE–QBOW temperature anomalies

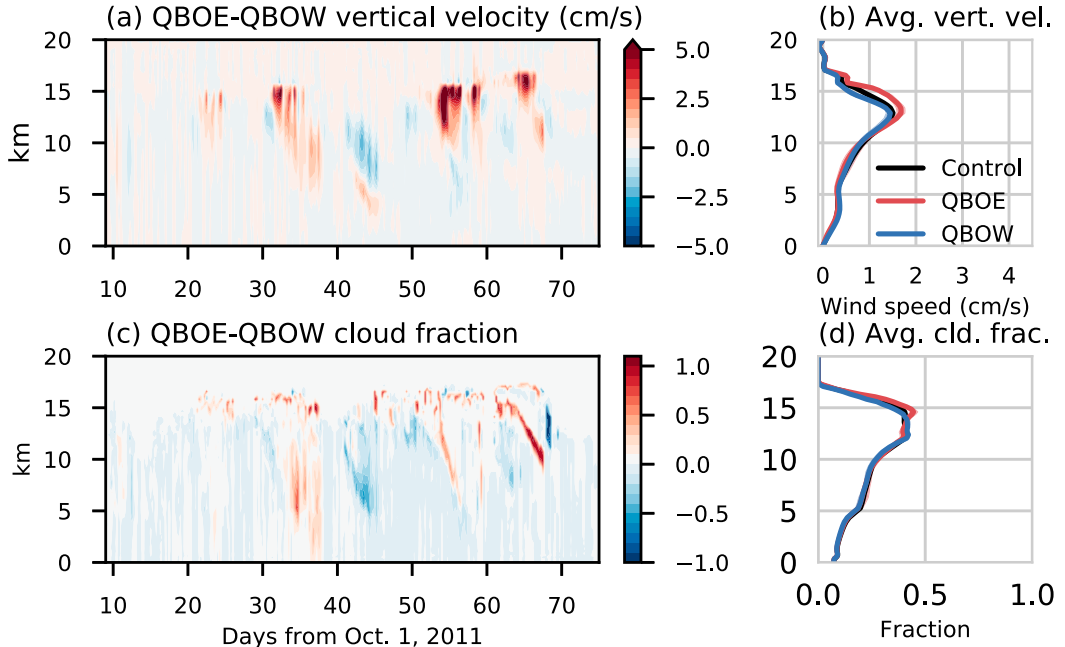


FIG. 10. From the same experiment as in Fig. 9, showing the horizontally averaged, ensemble-averaged QBOE–QBOW difference in (a),(b) vertical velocity and (c),(d) cloud fraction. As in Fig. 5, (b) and (d) show the time mean for the control, QBOE, and QBOW runs, with shading indicating ensemble spread.

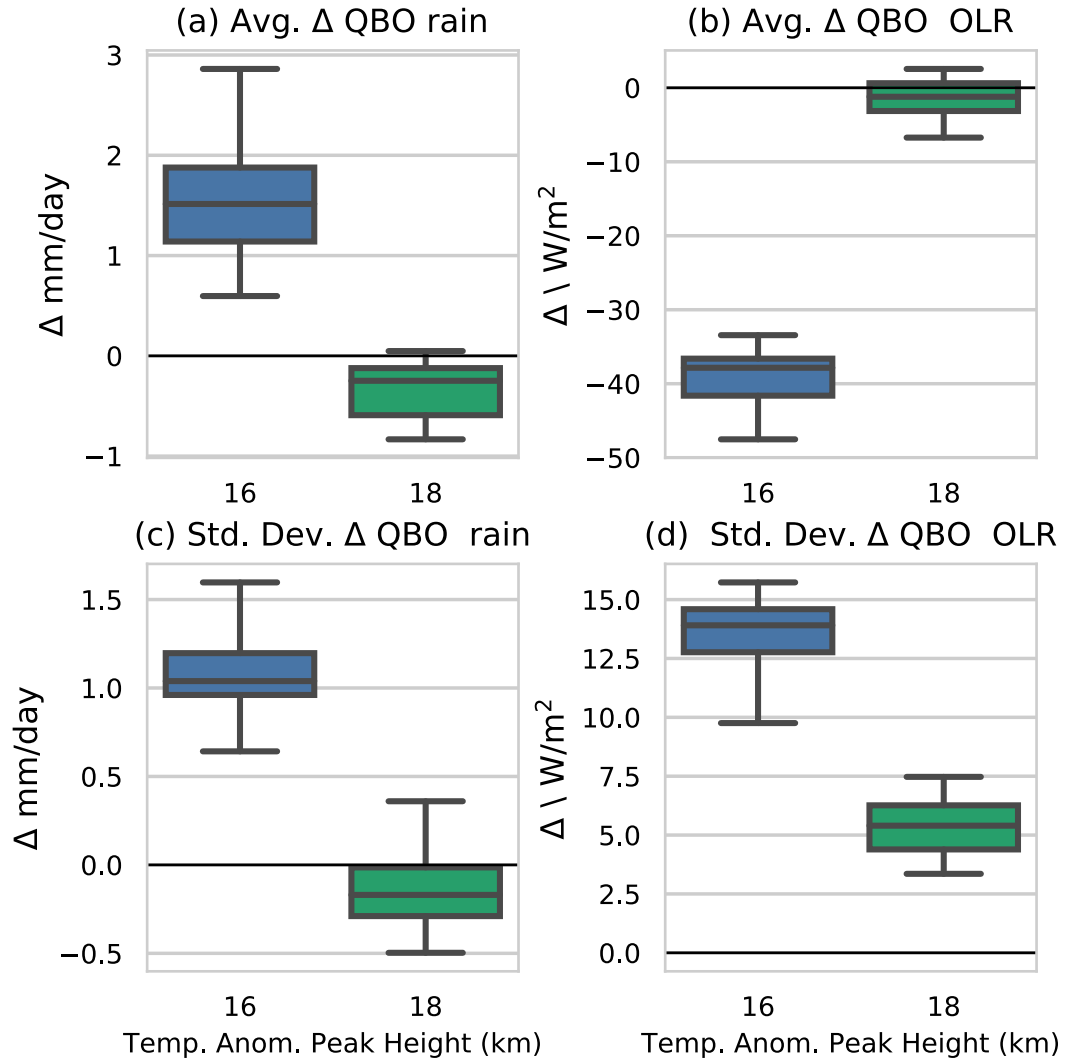


FIG. 11. QBOE–QBOW changes in the (top) mean and (bottom) standard deviation of domain-averaged (a),(c) rain and (b),(d) OLR in the 16- and 18-km-peaked temperature experiments. To capture the spread, the difference in the respective quantities was calculated for all 25 pairs of the 5 QBOE and 5 QBOW ensemble members. The box plots mark the median (center line), the upper and lower quartiles (box), and the range (whiskers).

with $M_t = \pm 0.5$ K in contrast have the weakest response relative to the control, while the “realistic” amplitude temperature anomalies with $M_t = \pm 1$ K have a response in between the ± 0.5 - and ± 2 -K results.

Despite being monotonic, the results do not appear strictly linear. For example, the QBOE–QBOW difference in vertical velocity, cloud fraction, and OLR is larger (smaller) when comparing the 2-K QBOE run (2-K QBOW run) to the control run than when comparing the 1-K QBOE and QBOW runs to one another (not shown). This is despite the fact that the total QBOE–QBOW anomaly is identical in each case. This suggests that the MJO response to the same QBO forcing may be stronger when the TTL is colder (i.e., that the MJO response may depend on the base state of the tropopause

region). However, given that the literature on the MJO–QBO relationship has not addressed the issue of the TTL base state, and given that this may simply be an artifact of our limited number of integrations or idealized model, we defer further exploration of this question to future work.

While the time-mean precipitation response is monotonic (Table 2), the time series in Fig. 12 shows that precipitation generally varies in a more complex manner across these integrations. The 2-K QBOE run, for example, rarely rains more than the 1- and 0.5-K QBOE runs, except in the periods following the MJO active phases. More significantly, the 2-K QBOW run completely misses the second MJO event, settling into the nonprecipitating state discussed in section 2c (see Fig. 12a at day 45). While the dry state is inconsistent

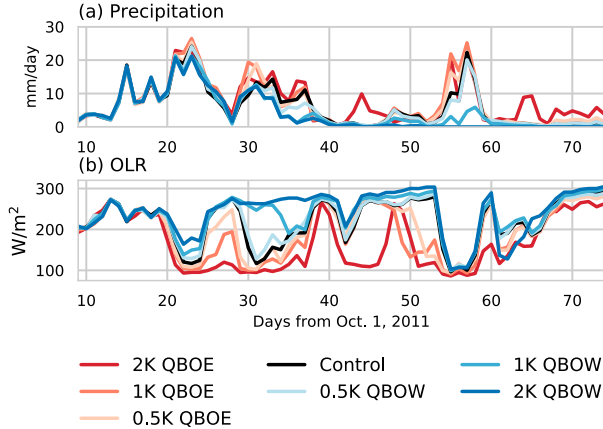


FIG. 12. Horizontally averaged (a) precipitation and (b) OLR from simulations varying the amplitude of the QBO temperature anomaly (all with $z_0 = 16$ km). Here darker red indicates a stronger QBOE anomaly and darker blue indicates stronger QBOW anomaly. The legend indicates the phase of the QBO and the magnitude of the QBO amplitude $|M_i|$. The control, 1-K QBOE, and 1-K QBOW runs are not the ensemble average as in Fig. 4, but a particular run chosen randomly from the five ensemble members, to facilitate comparison.

with the DYNAMO data and prohibits comparison to some degree, it is indicative of the ability of temperatures in the TTL to exert an influence on the troposphere (if too strongly so). That the precipitation time series across these experiments are less monotonic than other variables is consistent with findings already noted.

4. Discussion

Our results suggest that QBO-induced temperature anomalies in the tropical tropopause region can influence convection associated with the MJO, providing a likely pathway for the MJO–QBO relationship seen in observations. Our sensitivity experiments demonstrate that the height and the amplitude of the QBO temperature anomaly substantially affect the strength of the MJO convective response. These sensitivities are consistent qualitatively with Nie and Sobel's (2015) results on the QBO influence on convection in a statistically steady state, though their focus was not on the MJO. Both the pronounced sensitivity to the height of the temperature anomaly and the stronger model response to the QBO during the MJO active phases suggest that the QBO exerts an influence on the MJO primarily through an influence on convection sufficiently deep that it reaches the QBO temperature anomalies. This is consistent with other studies that show the QBO modulates convection in regions where such convection is already strong (e.g., Collimore et al. 2003; Liess and Geller 2012). It may also offer insight into why the MJO–QBO link only manifests in boreal winter, as MJO

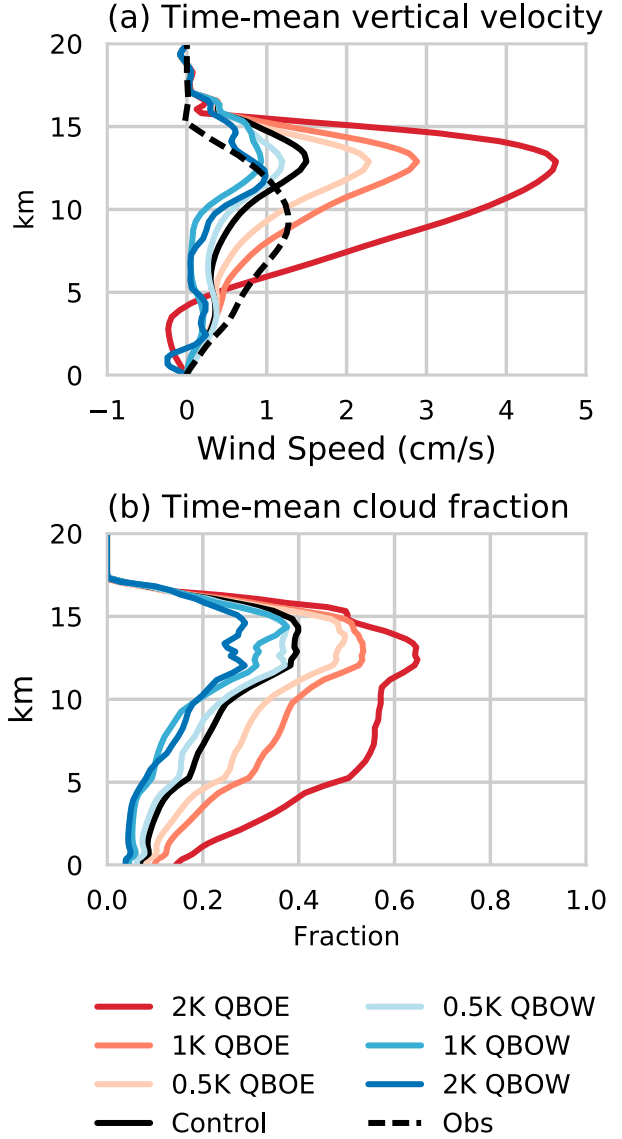


FIG. 13. As in Fig. 12, but showing the time-mean (a) vertical velocity and (b) cloud fraction. The observed vertical velocity is also shown in dashed black.

convection is known to be strongest during that season (e.g., Zhang 2013). This sensitivity of the QBO impact to the depth of convection could further explain why the observed QBO influence on the MJO seems strongest around the Maritime Continent (e.g., Son et al. 2017; Zhang and Zhang 2018). Our study, which is centered over the Indian Ocean, may underestimate the effect of the QBO on the MJO for this same reason, though we have not explored this possibility here.

Our results also show a sensitivity to the amplitude of the QBO temperature anomaly. This finding may be particularly applicable to the recent work by Lee and Klingaman (2018), who examined the MJO–QBO

TABLE 2. Time-mean, domain-averaged precipitation and outgoing longwave radiation for the seven experiments varying the amplitude of the QBO temperature anomaly. The first column indicates the amplitude of the QBO temperature anomaly, per Eq. (2).

List of experiments	Precipitation (mm day ⁻¹)	OLR (W m ⁻²)
QBOE ($M_t = -2$ K)	7.51	165
QBOE ($M_t = -1$ K)	7.02	193
QBOE ($M_t = -0.5$ K)	6.50	203
Control	5.97	220
QBOW ($M_t = 0.5$ K)	5.76	224
QBOW ($M_t = 1$ K)	4.49	237
QBOW ($M_t = 2$ K)	3.98	243

relationship in a GCM and found no significant link between the two phenomena. One of their hypotheses was that the GCM-simulated QBO temperature anomalies were too weak: less than one-fourth the magnitude of the observed anomaly (their Fig. 4). Our results here lend additional support to that hypothesis.

As seen in section 3c and below in the appendix, the response of MJO-related precipitation to the QBO state in our model is sensitive to the model configuration, and displays less monotonicity than other variables to variations in the height and amplitude of the QBO temperature anomaly. Precipitation also shows the greatest degree of variability between QBOE and QBOW. Given that Son et al. (2017) found a strong QBO signal in precipitation based on composites of the MJO in different QBO phases (their Fig. 3), this lack of a clear signal is difficult to reconcile with observations. However, Nie and Sobel (2015) found in their study imposing similar QBO anomalies in an idealized model that the QBOE–QBOW precipitation change was a nonmonotonic function of sea surface temperature. This nonmonotonicity resulted from a competition between changes in the gross moist stability (associated with changes in the vertical structure of the large-scale vertical motion) and radiative feedbacks, and suggests that precipitation changes may be more delicate than changes in other variables are. This may explain why, for example, in Fig. 7 we observe cases with notable changes to the vertical velocity and cloud fraction but small changes in precipitation. In these cases, changes to the radiative heating (e.g., warming due to an increase in high clouds) and changes in the amplitude and structure of the vertical velocity (e.g., toward a more top-heavy vertical velocity profile) may counteract one another. For a more nuanced discussion of the implications of these types of changes on precipitation, readers are referred to Nie and Sobel (2015, their section 3c).

Zhang and Zhang (2018) also looked more specifically at the question of the QBO influence on MJO-related precipitation in their observational study. They noted

that in the Indian Ocean, QBO changes to total precipitation were insignificant because of the canceling effects of precipitation associated with the MJO and non-MJO precipitation: non-MJO precipitation increases in QBOE whereas MJO precipitation decreases in QBOE. These results, in conjunction with our study, suggest the relationship between the QBO and MJO precipitation deserves more careful study. Other observational evidence further suggests it is important to distinguish between QBO changes to tropical mean convection and QBO changes to convection associated with the MJO. Son et al. (2017) showed that QBO changes to tropical mean OLR were not statistically significant, whereas QBO changes to the variance of OLR on MJO time scales were significant (see their Fig. 1). As other studies have found evidence for QBO changes to mean convection (i.e., Collimore et al. 2003; Liess and Geller 2012, Nie and Sobel 2015), more observational studies on this issue are needed.

In all our simulations in which the QBO has an influence on the MJO, that influence is strongest during the MJO active phase and weaker or of opposite sign during the suppressed phase. This strengthening of MJO convection primarily during the active phase leads to an increase in the variance on MJO time scales. Whether the mean state also changes because of the QBO depends on the relative sign and magnitude of changes in the active and suppressed phases. In several of our runs, especially the 16-km-peaked temperature experiment, we observe a change in the time mean of all the variables we consider, including OLR and precipitation. This seems inconsistent with the results of Son et al. (2017). However, our 65-day time period of integration makes separation of the mean state and MJO difficult. It may be that for longer integrations that simulate more MJO events and periods where no MJO is present, changes to the mean state like those seen in our study would be averaged out. Additionally, the 16- and 17-km-peaked runs have a larger QBO forcing than observed, making direct comparison with observations difficult. It may be that the strong response in these cases during the MJO active phase overwhelm changes during the suppressed phase, leading to a change in the mean. In runs with smaller forcing, such as the 18-km-peaked temperature experiments, the increase in the active phase is smaller, and is balanced in the mean by the decreases during the suppressed phase, leading to less change in the mean state while still allowing for a change in variance (i.e., Fig. 11).

5. Conclusions

In this study we examine the MJO–QBO relationship using a cloud-resolving model coupled to parameterized

large-scale dynamics. The goal is to explore whether the model can reproduce aspects of the observed MJO–QBO relationship; in particular, a strengthening (weakening) of MJO convection during the easterly (westerly) phase of the QBO. We also seek to identify likely pathways through which the QBO modulates the MJO. After establishing that our model reasonably reproduces two observed MJO events (Fig. 3), we conduct three types of experiments: 1) adding only QBOE or QBOW temperature signals to the large-scale forcing, 2) adding only QBOE or QBOW zonal wind signals, and 3) adding QBOE or QBOW temperature and wind signals together. These experiments were designed to isolate particular pathways of potential QBO influence. In addition, we conducted sensitivity experiments modifying the height and amplitude of the QBO anomalies (see Table 1). Our main results can be summarized as follows:

- 1) Forcing the model with idealized QBO temperature anomalies in the tropopause region (without the accompanying QBO wind anomalies) influences the simulated MJO convection in a manner qualitatively consistent with the observed MJO–QBO relationship: strengthening the MJO convection during QBOE and weakening it during QBOW (Figs. 4 and 5). This is evident across several variables, including cloud fraction, vertical velocity, precipitation, and outgoing longwave radiation.
- 2) QBO wind anomalies do not have a large effect on the model MJO convection (e.g., Fig. 7), either on their own or in combination with temperature anomalies, indicating that the dominant influence of the QBO on the simulated MJO convection is that due to QBO temperature anomalies.
- 3) The MJO response to the QBO depends significantly on the height and amplitude of the QBO temperature anomaly. Higher altitude or smaller-amplitude temperature anomalies lead to a weaker MJO response (e.g., Figs. 8 and 13). For “realistic” heights of the QBO temperature anomalies, the QBO influence on simulated MJO convection is smaller than that in cases with lower-than-observed anomalies, and for some variables (e.g., precipitation) it is inconclusive (Fig. 11).

Taken as a whole, our results suggest that the QBO-induced temperature anomalies are responsible for driving the majority of the MJO–QBO interaction. However, our results do not entirely explain the observed MJO–QBO relationship, and several caveats deserve further study. First, while the MJO response is clear and of the correct sign for larger-than-observed forcing, more realistic QBO temperature anomalies induce a smaller signal that is difficult to detect. Additionally, the model’s

precipitation response to the QBO is at times either absent or of the opposite sign to that initially expected (i.e., higher during QBOW rather than QBOE). Precipitation also displays nonmonotonic behavior with respect to QBO forcing parameters in our sensitivity testing, and the response is sensitive to the model configuration (see the appendix). While some modeling and observational studies suggest that this may not be entirely inconsistent with observations (Nie and Sobel 2015; Zhang and Zhang 2018) others indicate a strong observed precipitation signal (Son et al. 2017). Finally, in several simulations we observe QBO-induced changes not only to the variance of MJO convection, but also to the mean state. This seems inconsistent with the results of Son et al. (2017) and does not explain why MJO convection seems affected more strongly by the QBO than climatological convection. It is possible though that this difference is simply due to our short integration period (around 2.5 months), which makes separation of MJO and climatological time scales difficult.

Additional work is needed to verify our results, especially modeling studies that simulate more complex pathways of QBO influence or a more realistic interplay between the MJO and QBO. More specific hypotheses for the exact mechanism driving the MJO–QBO relationship, as well as extensions of this study, which increase the statistical robustness of our results, will be explored in future work.

Acknowledgments. The authors acknowledge support from NSF AGS-1543932.

APPENDIX

Sensitivity to SWTG Top

In this appendix we briefly examine the sensitivity of our results to the SWTG top boundary condition and vertical modes (see section 2b). We redo several QBO experiments using the SWTG modes recalculated with a rigid lid at 16 km rather than at 20 km. While this lower lid is closer to the observed vertical velocity in the DYNAMO data (see Fig. 1a), it may be overly restrictive, preventing the vertical velocity from responding to anomalies in the TTL. To place our rigid lid well above both the height of convection and the QBO anomalies we impose, and because choice of this parameter is not physically well constrained, we chose to use the 20-km boundary in the main text.

Figure A1 shows the OLR and precipitation time series from these integrations, which are identical to the 16-km-peaked, temperature-only run in section 3b except for changes to the modes/rigid lid. The general sign

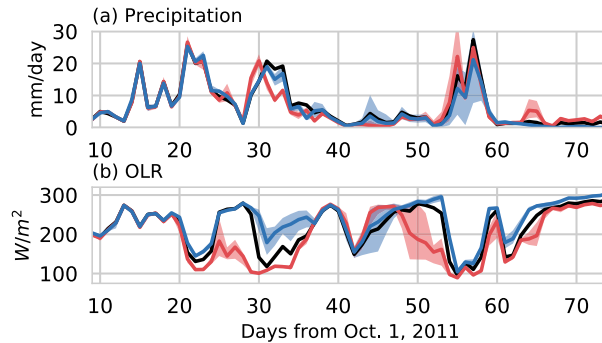


FIG. A1. As in Fig. 4, but altering the spectral weak temperature gradient vertical modes and vertical velocity such that the model has a rigid lid at 16 km, as opposed to the 20-km rigid lid used in the main text.

and magnitude of QBOE–QBOW differences are not markedly different from the higher lid cases in the vertical velocity and cloud fraction and thus are not shown. However, the precipitation no longer increases significantly during QBOE relative to QBOW: during the first MJO event there are some periods where QBOE precipitates more (e.g., ~days 23 and 29) and others where QBOW precipitates more (e.g., ~day 33). The same is true for the second MJO event. This lack of consistency even within individual events indicates that the precipitation response to the QBO in this model is sensitive to the model configuration and is less consistent than other variables in showing enhanced convection in QBOE compared to QBOW.

REFERENCES

- Anber, U., S. Wang, and A. Sobel, 2017: Coupling with ocean mixed layer leads to intraseasonal variability in tropical deep convection: Evidence from cloud-resolving simulations. *J. Adv. Model. Earth Syst.*, **9**, 616–626, <https://doi.org/10.1002/2016MS000803>.
- Baldwin, M. P., and Coauthors, 2001: The quasi-biennial oscillation. *Rev. Geophys.*, **39**, 179–229, <https://doi.org/10.1029/1999RG000073>.
- Bergman, J., and P. D. Sardeshmukh, 2004: Dynamic stabilization of atmospheric single column models. *J. Climate*, **17**, 1004–1021, [https://doi.org/10.1175/1520-0442\(2004\)017<1004:DSOASC>2.0.CO;2](https://doi.org/10.1175/1520-0442(2004)017<1004:DSOASC>2.0.CO;2).
- Blossey, P. N., C. S. Bretherton, J. Cetrone, and M. Khairoutdinov, 2007: Cloud-resolving model simulations of KWAJEX: Model sensitivities and comparisons with satellite and radar observations. *J. Atmos. Sci.*, **64**, 1488–1508, <https://doi.org/10.1175/JAS3982.1>.
- Bony, S., and K. A. Emanuel, 2005: On the role of moist processes in tropical intraseasonal variability: Cloud–radiation and moisture–convection feedbacks. *J. Atmos. Sci.*, **62**, 2770–2789, <https://doi.org/10.1175/JAS3506.1>.
- Bretherton, C. S., and P. K. Smolarkiewicz, 1989: Gravity waves, compensating subsidence, and entrainment and detrainment around cumulus clouds. *J. Atmos. Sci.*, **46**, 740–759, [https://doi.org/10.1175/1520-0469\(1989\)046<0740:GWCSAD>2.0.CO;2](https://doi.org/10.1175/1520-0469(1989)046<0740:GWCSAD>2.0.CO;2).
- Charney, J. G., 1963: A note on large-scale motions in the tropics. *J. Atmos. Sci.*, **20**, 607–609, [https://doi.org/10.1175/1520-0469\(1963\)020<0607:ANOLSM>2.0.CO;2](https://doi.org/10.1175/1520-0469(1963)020<0607:ANOLSM>2.0.CO;2).
- Chou, M.-D., and M. J. Suarez, 1999: A solar radiation parameterization for atmospheric studies. NASA Tech. Rep. NASA/TM-1999-10460, Vol. 15, NASA, Washington, DC, 38 pp.
- Collimore, C. C., D. W. Martin, M. H. Hitchman, A. Huesmann, and D. E. Waliser, 2003: On the relationship between the QBO and tropical deep convection. *J. Climate*, **16**, 2552–2568, [https://doi.org/10.1175/1520-0442\(2003\)016<2552:OTRBTQ>2.0.CO;2](https://doi.org/10.1175/1520-0442(2003)016<2552:OTRBTQ>2.0.CO;2).
- Crueger, T., and B. Stevens, 2015: The effect of atmospheric radiative heating by clouds on the Madden-Julian oscillation. *J. Adv. Model. Earth Syst.*, **7**, 854–864, <https://doi.org/10.1002/2015MS000434>.
- Daleu, C. L., and Coauthors, 2015: Intercomparison of methods of coupling between convection and large-scale circulation: 1. Comparison over uniform surface conditions. *J. Adv. Model. Earth Syst.*, **7**, 1576–1601, <https://doi.org/10.1002/2015MS000468>.
- , and Coauthors, 2016: Intercomparison of methods of coupling between convection and large-scale circulation: 2. Comparison over nonuniform surface conditions. *J. Adv. Model. Earth Syst.*, **8**, 387–405, <https://doi.org/10.1002/2015MS000570>.
- Dee, D. P., and Coauthors, 2011: The ERA-Interim reanalysis: Configuration and performance of the data assimilation system. *Quart. J. Roy. Meteor. Soc.*, **137**, 553–597, <https://doi.org/10.1002/qj.828>.
- Edman, J. P., and D. M. Romps, 2014: An improved weak pressure gradient scheme for single-column modeling. *J. Atmos. Sci.*, **71**, 2415–2429, <https://doi.org/10.1175/JAS-D-13-0327.1>.
- , and —, 2015: Self-consistency tests of large-scale dynamics parameterizations for single-column modeling. *J. Adv. Model. Earth Syst.*, **7**, 320–334, <https://doi.org/10.1002/2014MS000378>.
- Emanuel, K., A. A. Wing, and E. M. Vincent, 2014: Radiative-convective instability. *J. Adv. Model. Earth Syst.*, **6**, 75–90, <https://doi.org/10.1002/2013MS000270>.
- Fulton, S. R., and W. H. Schubert, 1985: Vertical normal transforms: Theory and application. *Mon. Wea. Rev.*, **113**, 647–658, [https://doi.org/10.1175/1520-0493\(1985\)113<0647:VNMTTA>2.0.CO;2](https://doi.org/10.1175/1520-0493(1985)113<0647:VNMTTA>2.0.CO;2).
- Garfinkel, C. I., and D. L. Hartmann, 2011: The influence of the quasi-biennial oscillation on the troposphere in winter in a hierarchy of models. Part I: Simplified dry GCMs. *J. Atmos. Sci.*, **68**, 1273–1289, <https://doi.org/10.1175/2011JAS3665.1>.
- Giorgetta, M. A., L. Bengtsson, and K. Arpe, 1999: An investigation of QBO signals in the East Asian and Indian monsoon in GCM experiments. *Climate Dyn.*, **15**, 435–450, <https://doi.org/10.1007/s003820050292>.
- Grabowski, W. W., X. Wu, and M. W. Moncrieff, 1996: Cloud resolving modeling of tropical cloud systems during Phase III of GATE. Part I: Two-dimensional experiments. *J. Atmos. Sci.*, **53**, 3684–3709, [https://doi.org/10.1175/1520-0469\(1996\)053<3684:CRMOTC>2.0.CO;2](https://doi.org/10.1175/1520-0469(1996)053<3684:CRMOTC>2.0.CO;2).
- Gray, W. M., J. D. Sheaffer, and J. A. Knaff, 1992a: Hypothesized mechanism for stratospheric QBO influence on ENSO variability. *Geophys. Res. Lett.*, **19**, 107–110, <https://doi.org/10.1029/91GL02950>.
- , —, and —, 1992b: Influence of the stratospheric QBO on ENSO variability. *J. Meteor. Soc. Japan*, **70**, 975–995, https://doi.org/10.2151/jmsj1965.70.5_975.
- Hartmann, D. L., J. R. Holton, and Q. Fu, 2001: The heat balance of the tropical tropopause, cirrus, and stratospheric dehydration.

- Geophys. Res. Lett.*, **28**, 1969–1972, <https://doi.org/10.1029/2000GL012833>.
- Held, I. M., and B. J. Hoskins, 1985: Large-scale eddies and the general circulation of the troposphere. *Advances in Geophysics*, Vol. 28, Academic Press, 3–31.
- Hendon, H. H., and S. Abhik, 2018: Differences in vertical structure of the Madden-Julian oscillation associated with the quasi-biennial oscillation. *Geophys. Res. Lett.*, **45**, 4419–4428, <https://doi.org/10.1029/2018GL077207>.
- Herman, M. J., and D. J. Raymond, 2014: WTG cloud modeling with spectral decomposition of heating. *J. Adv. Model. Earth Syst.*, **6**, 1121–1140, <https://doi.org/10.1002/2014MS000359>.
- Holton, J. R., and R. S. Lindzen, 1972: An updated theory for the quasi-biennial cycle of the tropical stratosphere. *J. Atmos. Sci.*, **29**, 1076–1080, [https://doi.org/10.1175/1520-0469\(1972\)029<1076:AUTFTQ>2.0.CO;2](https://doi.org/10.1175/1520-0469(1972)029<1076:AUTFTQ>2.0.CO;2).
- Hong, S.-Y., Y. Noh, and J. Dudhia, 2006: A new vertical diffusion package with an explicit treatment of entrainment processes. *Mon. Wea. Rev.*, **134**, 2318–2341, <https://doi.org/10.1175/MWR3199.1>.
- Hong, Y., G. Liu, and J.-L. F. Li, 2016: Assessing the radiative effects of global ice clouds based on CloudSat and CALIPSO measurements. *J. Climate*, **29**, 7651–7674, <https://doi.org/10.1175/JCLI-D-15-0799.1>.
- Hood, L. L., 2017: QBO/solar modulation of the boreal winter Madden-Julian oscillation: A prediction for the coming solar minimum. *Geophys. Res. Lett.*, **44**, 3849–3857, <https://doi.org/10.1002/2017GL072832>.
- Iacono, M. J., J. S. Delamere, E. J. Mlawer, M. W. Shephard, S. A. Clough, and W. D. Collins, 2008: Radiative forcing by long-lived greenhouse gases: Calculations with the AER radiative transfer models. *J. Geophys. Res.*, **113**, D13103, <https://doi.org/10.1029/2008JD009944>.
- Johnson, R. H., and P. E. Ciesielski, 2013: Structure and properties of Madden-Julian oscillations deduced from DYNAMO sounding arrays. *J. Atmos. Sci.*, **70**, 3157–3179, <https://doi.org/10.1175/JAS-D-13-065.1>.
- , —, J. H. Ruppert, and M. Katsumata, 2015: Sounding-based thermodynamic budgets for DYNAMO. *J. Atmos. Sci.*, **72**, 598–622, <https://doi.org/10.1175/JAS-D-14-0202.1>.
- Klemp, J. B., J. Dudhia, and A. D. Hassiotis, 2008: An upper gravity-wave absorbing layer for NWP applications. *Mon. Wea. Rev.*, **136**, 3987–4004, <https://doi.org/10.1175/2008MWR2596.1>.
- Kuang, Z., 2008: Modeling the interaction between cumulus convection and linear gravity waves using a limited-domain cloud system-resolving model. *J. Atmos. Sci.*, **65**, 576–591, <https://doi.org/10.1175/2007JAS2399.1>.
- Kuma, K.-I., 1990: A quasi-biennial oscillation in the intensity of the intra-seasonal oscillation. *Int. J. Climatol.*, **10**, 263–278, <https://doi.org/10.1002/joc.3370100304>.
- Lee, J. C. K., and N. P. Klingaman, 2018: The effect of the quasi-biennial oscillation on the Madden-Julian oscillation in the Met Office Unified Model Global Ocean Mixed Layer configuration. *Atmos. Sci. Lett.*, **19**, e816, <https://doi.org/10.1002/asl.816>.
- Li, X., and Coauthors, 2018: Evolution of precipitation structure during the November DYNAMO MJO event: Cloud-resolving model intercomparison and cross validation using radar observations. *J. Geophys. Res. Atmos.*, **123**, 3530–3555, <https://doi.org/10.1002/2017JD027775>.
- Liess, S., and M. A. Geller, 2012: On the relationship between QBO and distribution of tropical deep convection. *J. Geophys. Res. Atmos.*, **117**, D03108, <https://doi.org/10.1029/2011JD016317>.
- Lindzen, R. S., and J. R. Holton, 1968: A theory of the quasi-biennial oscillation. *J. Atmos. Sci.*, **25**, 1095–1107, [https://doi.org/10.1175/1520-0469\(1968\)025<1095:ATOTQB>2.0.CO;2](https://doi.org/10.1175/1520-0469(1968)025<1095:ATOTQB>2.0.CO;2).
- Madden, R. A., and P. R. Julian, 1994: Observations of the 40–50-day tropical oscillation—A review. *Mon. Wea. Rev.*, **122**, 814–837, [https://doi.org/10.1175/1520-0493\(1994\)122<0814:OOTDTO>2.0.CO;2](https://doi.org/10.1175/1520-0493(1994)122<0814:OOTDTO>2.0.CO;2).
- Mapes, B. E., 1997: What controls large-scale variations of deep convection? *Proc. Workshop on New Insights and Approaches to Cumulus Parameterization*, Reading, United Kingdom, ECMWF, 157–165.
- , 2004: Sensitivities of cumulus ensemble rainfall in a cloud-resolving model with parameterized large-scale dynamics. *J. Atmos. Sci.*, **61**, 2308–2317, [https://doi.org/10.1175/1520-0469\(2004\)061<2308:SOCRIA>2.0.CO;2](https://doi.org/10.1175/1520-0469(2004)061<2308:SOCRIA>2.0.CO;2).
- , and P. Zuidema, 1996: Radiative-dynamical consequences of dry tongues in the tropical troposphere. *J. Atmos. Sci.*, **53**, 620–638, [https://doi.org/10.1175/1520-0469\(1996\)053<0620:RDCODT>2.0.CO;2](https://doi.org/10.1175/1520-0469(1996)053<0620:RDCODT>2.0.CO;2).
- Marshall, A. G., H. H. Hendon, S.-W. Son, and Y. Lim, 2017: Impact of the quasi-biennial oscillation on predictability of the Madden-Julian oscillation. *Climate Dyn.*, **49**, 1365–1377, <https://doi.org/10.1007/s00382-016-3392-0>.
- Matsui, T., W.-K. Tao, and R. Shi, 2007: Goddard radiation and aerosol direct effect in Goddard WRF. *NASA/UMD WRF Workshop*, College Park, MD, NASA and University of Maryland, College Park, 12 pp.
- Morrison, H., G. Thompson, and V. Tatarskii, 2009: Impact of cloud microphysics on the development of trailing stratiform precipitation in a simulated squall line: Comparison of one- and two-moment schemes. *Mon. Wea. Rev.*, **137**, 991–1007, <https://doi.org/10.1175/2008MWR2556.1>.
- Nie, J., and A. H. Sobel, 2015: Responses of tropical deep convection to the QBO: Cloud-resolving simulations. *J. Atmos. Sci.*, **72**, 3625–3638, <https://doi.org/10.1175/JAS-D-15-0035.1>.
- , and —, 2016: Modeling the interaction between quasi-geostrophic vertical motion and convection in a single column. *J. Atmos. Sci.*, **73**, 1101–1117, <https://doi.org/10.1175/JAS-D-15-0205.1>.
- Nishimoto, E., and S. Yoden, 2017: Influence of the stratospheric quasi-biennial oscillation on the Madden-Julian oscillation during austral summer. *J. Atmos. Sci.*, **74**, 1105–1125, <https://doi.org/10.1175/JAS-D-16-0205.1>.
- Plumb, R. A., and D. McEwan, 1978: The instability of a forced standing wave in a viscous stratified fluid: A laboratory analogue of the quasi-biennial oscillation. *J. Atmos. Sci.*, **35**, 1827–1839, [https://doi.org/10.1175/1520-0469\(1978\)035<1827:TIOAFS>2.0.CO;2](https://doi.org/10.1175/1520-0469(1978)035<1827:TIOAFS>2.0.CO;2).
- Raymond, D. J., and X. Zeng, 2005: Modelling tropical atmospheric convection in the context of the weak temperature gradient approximation. *Quart. J. Roy. Meteor. Soc.*, **131**, 1301–1320, <https://doi.org/10.1256/qj.03.97>.
- Romps, D., 2012a: Numerical tests of the weak pressure gradient approximation. *J. Atmos. Sci.*, **69**, 2846–2856, <https://doi.org/10.1175/JAS-D-11-0337.1>.
- , 2012b: Weak pressure gradient approximation and its analytical solutions. *J. Atmos. Sci.*, **69**, 2835–2845, <https://doi.org/10.1175/JAS-D-11-0336.1>.
- Sentíć, S., S. L. Sessions, and Z. Fuchs, 2015: Diagnosing DYNAMO convection with weak temperature gradient simulations. *J. Adv. Model. Earth Syst.*, **7**, 1849–1871, <https://doi.org/10.1002/2015MS000531>.
- Sessions, S. L., S. Sugaya, D. J. Raymond, and A. H. Sobel, 2010: Multiple equilibria in a cloud-resolving model using the weak

- temperature gradient approximation. *J. Geophys. Res.*, **115**, D12110, <https://doi.org/10.1029/2009JD013376>.
- , S. Sentić, and M. J. Herman, 2016: The role of radiation in organizing convection in weak temperature gradient simulations. *J. Adv. Model. Earth Syst.*, **8**, 244–271, <https://doi.org/10.1002/2015MS000587>.
- Shi, J. J., and Coauthors, 2010: WRF simulations of the 20–22 January 2007 snow events over eastern Canada: Comparison with in situ and satellite observations. *J. Appl. Meteor. Climatol.*, **49**, 2246–2266, <https://doi.org/10.1175/2010JAMC2282.1>.
- Skamarock, W. C., and Coauthors, 2008: A description of the Advanced Research WRF version 3. NCAR Tech. Note NCAR/TN-475+STR, 113 pp., <https://doi.org/10.5065/D68S4MVH>.
- Sobel, A. H., and C. S. Bretherton, 2000: Modeling tropical precipitation in a single column. *J. Climate*, **13**, 4378–4392, [https://doi.org/10.1175/1520-0442\(2000\)013<4378:MTPIAS>2.0.CO;2](https://doi.org/10.1175/1520-0442(2000)013<4378:MTPIAS>2.0.CO;2).
- , and E. D. Maloney, 2012: An idealized semi-empirical framework for modeling the Madden–Julian oscillation. *J. Atmos. Sci.*, **69**, 1691–1705, <https://doi.org/10.1175/JAS-D-11-0118.1>.
- , and —, 2013: Moisture modes and the eastward propagation of the MJO. *J. Atmos. Sci.*, **70**, 187–192, <https://doi.org/10.1175/JAS-D-12-0189.1>.
- , G. Bellon, and J. Bacmeister, 2007: Multiple equilibria in a single-column model of the tropical atmosphere. *Geophys. Res. Lett.*, **34**, L22804, <https://doi.org/10.1029/2007GL031320>.
- , S. Wang, and D. Kim, 2014: Moist static energy budget of the MJO during DYNAMO. *J. Atmos. Sci.*, **71**, 4276–4291, <https://doi.org/10.1175/JAS-D-14-0052.1>.
- Son, S.-W., Y. Lim, C. Yoo, H. H. Hendon, and J. Kim, 2017: Stratospheric control of Madden–Julian oscillation. *J. Climate*, **30**, 1909–1922, <https://doi.org/10.1175/JCLI-D-16-0620.1>.
- Tao, W.-K., D. Johnson, C.-L. Shie, and J. Simpson, 2004: The atmospheric energy budget and large-scale precipitation efficiency of convective systems during TOGA COARE, GATE, SCSMEX, and ARM: Cloud-resolving model simulations. *J. Atmos. Sci.*, **61**, 2405–2423, [https://doi.org/10.1175/1520-0469\(2004\)061<2405:TAEBAL>2.0.CO;2](https://doi.org/10.1175/1520-0469(2004)061<2405:TAEBAL>2.0.CO;2).
- Tulich, S. N., D. A. Randall, and B. E. Mapes, 2007: Vertical-mode and cloud decomposition of large-scale convectively coupled gravity waves in a two-dimensional cloud-resolving model. *J. Atmos. Sci.*, **64**, 1210–1229, <https://doi.org/10.1175/JAS3884.1>.
- Wang, J., H.-M. Kim, E. K. M. Chang, and S.-W. Son, 2018: Modulation of the MJO and North Pacific storm track relationship by the QBO. *J. Geophys. Res. Atmos.*, **123**, 3976–3992, <https://doi.org/10.1029/2017JD027977>.
- Wang, S., and A. H. Sobel, 2011: Response of convection to relative sea surface temperature: Cloud-resolving simulations in two and three dimensions. *J. Geophys. Res.*, **116**, D11119, <https://doi.org/10.1029/2010JD015347>.
- , —, and Z. Kuang, 2013: Cloud-resolving simulation of TOGA-COARE using parameterized large-scale dynamics. *J. Geophys. Res. Atmos.*, **118**, 6290–6301, <https://doi.org/10.1002/jgrd.50510>.
- , —, A. Fridlind, Z. Feng, J. Comstock, P. Minnis, and M. Nordeen, 2015: Simulations of cloud-radiation interaction using large-scale forcing derived from the CINDY/DYNAMO northern sounding array. *J. Adv. Model. Earth Syst.*, **7**, 1472–1498, <https://doi.org/10.1002/2015MS000461>.
- , —, and J. Nie, 2016: Modeling the MJO in a cloud-resolving model with parameterized large-scale dynamics: Vertical structure, radiation, and horizontal advection of dry air. *J. Adv. Model. Earth Syst.*, **8**, 121–139, <https://doi.org/10.1002/2015MS000529>.
- Wu, X., W. W. Grabowski, and M. W. Moncrieff, 1998: Long-term behavior of cloud systems in TOGA COARE and their interactions with radiative and surface processes. Part I: Two-dimensional modeling study. *J. Atmos. Sci.*, **55**, 2693–2714, [https://doi.org/10.1175/1520-0469\(1998\)055<2693:LTBOCS>2.0.CO;2](https://doi.org/10.1175/1520-0469(1998)055<2693:LTBOCS>2.0.CO;2).
- Wu, Z., E. S. Sarachik, and D. S. Battisti, 2000: Vertical structure of convective heating and the three-dimensional structure of the forced circulation on an equatorial beta plane. *J. Atmos. Sci.*, **57**, 2169–2187, [https://doi.org/10.1175/1520-0469\(2000\)057<2169:VSOCHA>2.0.CO;2](https://doi.org/10.1175/1520-0469(2000)057<2169:VSOCHA>2.0.CO;2).
- Yang, Q., Q. Fu, and Y. Hu, 2010: Radiative impacts of clouds in the tropical tropopause layer. *J. Geophys. Res.*, **115**, D00H12, <https://doi.org/10.1029/2009JD012393>.
- Yoneyama, K., C. Zhang, and C. N. Long, 2013: Tracking pulses of the Madden–Julian oscillation. *Bull. Amer. Meteor. Soc.*, **94**, 1871–1891, <https://doi.org/10.1175/BAMS-D-12-00157.1>.
- Yoo, C., and S.-W. Son, 2016: Modulation of the boreal wintertime Madden–Julian oscillation by the stratospheric quasi-biennial oscillation. *Geophys. Res. Lett.*, **43**, 1392–1398, <https://doi.org/10.1002/2016GL067762>.
- Yu, L., and R. A. Weller, 2007: Objectively analyzed air–sea heat fluxes for the global ice-free oceans (1981–2005). *Bull. Amer. Meteor. Soc.*, **88**, 527–539, <https://doi.org/10.1175/BAMS-88-4-527>.
- , X. Jin, and R. A. Weller, 2008: Multidecade Global Flux Datasets from the Objectively Analyzed Air–Sea Fluxes (OAFlux) Project: Latent and sensible heat fluxes, ocean evaporation, and related surface meteorological variables. OAFlux Project Tech. Rep. OA-2008-01, Woods Hole Oceanographic Institution, Woods Hole, MA, 64 pp., http://oafux.whoi.edu/pdfs/OAFlux_TechReport_3rd_release.pdf.
- Zhang, C., 2005: Madden–Julian oscillation. *Rev. Geophys.*, **43**, RG2003, <https://doi.org/10.1029/2004RG000158>.
- , 2013: Madden–Julian oscillation: Bridging weather and climate. *Bull. Amer. Meteor. Soc.*, **94**, 1849–1870, <https://doi.org/10.1175/BAMS-D-12-00026.1>.
- , and B. Zhang, 2018: QBO–MJO connection. *J. Geophys. Res. Atmos.*, **123**, 2957–2967, <https://doi.org/10.1002/2017JD028171>.